Cell arrangement impacts metabolic activity and antibiotic tolerance in *Pseudomonas aeruginosa* biofilms

Short title: Biofilm microanatomy influences physiological stratification

Hannah Dayton[a], Julie Kiss[a], Mian Wei[b], Shradha Chauhan[a], Emily LaMarre[c], William Cole Cornell[a], Chase J. Morgan[a], Anuradha Janakiraman[c], Wei Min[b], Raju Tomer[a], Alexa Price-Whelan[a], Jasmine A Nirody[d], Lars E.P. Dietrich[a]*

[a]Department of Biological Sciences, Columbia University, New York, NY 10025

[b]Department of Chemistry, Columbia University, New York, NY 10025

[c]Program in Biology, The Graduate Center, City University of New York, New York, NY 10016

[d]Department of Organismal Biology and Anatomy, University of Chicago, Chicago, Illinois 60637

*Corresponding author: Lars E.P. Dietrich
Email: LDietrich@columbia.edu

Competing Interest Statement: The authors declare no competing interest.

Classification: Biological Sciences (major), Microbiology (minor)

Keywords: biofilm physiology, metabolic heterogeneity, motility

ABSTRACT

Cells must access resources to survive, and the anatomy of multicellular structures influences this access. In diverse multicellular eukaryotes, resources are provided by internal conduits that allow substances to travel more readily through tissue than they would via diffusion. Microbes growing in multicellular structures, called biofilms, are also affected by differential access to resources and we hypothesized that this is influenced by the physical arrangement of the cells. In this study, we examined the microanatomy of biofilms formed by the pathogenic bacterium *Pseudomonas aeruginosa* and discovered that clonal cells form striations that are packed lengthwise across most of a mature biofilm's depth. We identified mutants, including those defective in pilus function and in O-antigen attachment, that show alterations to this lengthwise packing phenotype. Consistent with the notion that cellular arrangement affects access to resources within the biofilm, we found that while the wild type shows even distribution of tested substrates across depth, the mutants show accumulation of substrates at the biofilm boundaries. Furthermore, we found that altered cellular arrangement within biofilms affects the localization of metabolic activity, the survival of resident cells, and the susceptibility of subpopulations to antibiotic treatment. Our observations provide insight into cellular features that determine biofilm microanatomy, with consequences for physiological differentiation and drug sensitivity.

INTRODUCTION

Chemical gradients form inevitably during multicellular growth, leading to the establishment of distinct subzones–with different conditions of resource availability–in cellular aggregates and complex organisms [1]. The conditions of these subzones are important because they promote physiological differentiation, in turn affecting morphogenesis, metabolic activity, and susceptibility to drugs [2–6]. The capacity for substrate uptake and transport are therefore critical features of a cellular aggregate that are linked to structural development and our ability to treat disease, with diverse mechanisms controlling these processes in various multicellular structures and organisms. Many macroscopic eukaryotes, for example, contain circulatory systems in which specialized cells form conduits that deliver water and other resources to cells [7]. These specialized transport systems allow for efficient nutrient allocation, enabling multicellular organisms to grow, develop, and maintain homeostasis.

The predominant multicellular structure of the microbial world is the biofilm, an aggregate of cells attached to each other and encased in a self-produced matrix [8]. There have been many studies that have uncovered the presence and importance of spatial organization within the biofilm [9–17]. Biofilms often form at interfaces and are subject to steep external and internal chemical gradients, raising questions about how nutrients are allocated efficiently within these structures. While evidence suggests that passive diffusion through the matrix is a significant mechanism of resource distribution within biofilms [18,19] observations of biofilms formed by model microbes also indicate that morphological features and differentiation could impact substrate transport [20–23].

In this study, we examined the cellular-level anatomy of macrocolonies formed by the bacterium *Pseudomonas aeruginosa*, which is a major cause of biofilm-based and chronic infections in immunocompromised individuals [24]. We found that *P. aeruginosa* biofilms contain vertically arranged zones that differ with respect to cellular orientation and the proximity of related cells. Genetic analyses and microscopic imaging allowed us to identify cell surface components required for this patterning. Importantly, these approaches also revealed that cellular orientation impacts substrate uptake and distribution across the biofilm. Additional analysis via stimulated Raman scattering (SRS) microscopy and an assay for cell death uncovered correlations between cellular-arrangement subzones, physiological status, and susceptibility to antibiotic treatment. Collectively, these data link microanatomy to metabolic differentiation--and its consequences for survival and drug resilience—within maturing biofilms.

RESULTS AND DISCUSSION

Mature *P. aeruginosa* biofilms contain vertical, clonal striations

Growth at surface-air interfaces has been used for decades to guide treatment decisions made in the clinical setting and is a focus of research into *P. aeruginosa* biofilm development [25–34]. In particular, our group and others have used macrocolony biofilms as models to study the molecular links between resource availability and multicellular physiology [35–38]; we have discovered a variety of pathways and mechanisms that support the biofilm lifestyle, some of

which contribute to pathogenicity and antibiotic tolerance [39,40]. Macrocolony biofilms are formed when 1-10 uL of a cell suspension are pipetted onto agar-solidified media and incubated for several days (**Figure 1A**). The macrocolony biofilm model provides a high-throughput, macroscopic readout for the effects of a broad variety of factors–such as polysaccharide production, pilus function, and second messenger levels–that affect *P. aeruginosa* biofilm development [41–43]. It also provides a reproducible system for growing a physiologically differentiated multicellular structure that is amenable to techniques for mapping variations in extra- and intracellular chemistry, gene expression, and metabolic activity in situ [40,44–47].

Despite the significance of the macrocolony model to our understanding of *P. aeruginosa* biology, we lack detailed information about how cells are arranged within these structures and the genetic determinants of this arrangement. To begin to address this gap, we used scanning electron microscopy (SEM) to examine a WT *P. aeruginosa* PA14 macrocolony biofilm that had grown for 3 days on 1% tryptone, 1% agar. SEM images revealed two distinct zones, containing either "disordered" cells (in various orientations) or "ordered" cells (aligned lengthwise) (**Figure 1A**). Similar arrangements of cells aligned lengthwise with ordered packing have been described for diverse bacterial systems [11,48–56].

To assess the distribution of clonal (related) cells in the ordered region, we grew macrocolony biofilms in a “mixing assay” in which the inoculum contained 2.5% of a strain that constitutively expresses mScarlet as a fluorescent marker ($P_{PA1/04/03}$-*mScarlet*). (The remaining 97.5% of the cell population was unmarked.) Biofilms were embedded in paraffin and thin-sectioned, and sections taken from the colony center (**Figure 1A**) were imaged by fluorescence microscopy [57] (**Figure 1B**). We discovered that fluorescent cells within the disordered region (zone 1) are randomly dispersed, while fluorescent cells in the ordered region are arranged in evenly spaced vertical striations reminiscent of the cellular packing seen in the SEM images (**Figure 1A**). To determine their orientations, we used a custom Python script that allowed us to detect individual cells and plot their angles relative to the vertical axis across biofilm depth. While the fluorescent cells in zone 1 are randomly oriented, those in zone 2 are oriented along the vertical axis, consistent with the arrangements visible by SEM (**Figure 1A**). Finally, in the uppermost portion of the biofilm (zone 3), cell orientation shows increased deviation from the vertical alignment, though fluorescent cells still appear to be spatially aggregated (**Figure 1B**).

Growth at the liquid-air interface constitutes another popular model system that has provided insights into mechanisms of biofilm formation [30,33,58,59]. To examine whether striated arrangement, similar to that observed in the macrocolony biofilm, develops in a biofilm grown at the liquid-air interface (pellicle) we used the same ratio of marked and unmarked cells as inocula for pellicle biofilm cultures. After three days of growth, pellicle biofilms were transferred to agar-solidified media and immediately embedded in paraffin and thin-sectioned. Microscopic analysis revealed that mixing-assay pellicle biofilms also show fluorescent striations (**Figure 1D**). Each of the pellicles imaged showed striations covering most or all of the biofilm depth and containing cells in random orientations. Together, these findings demonstrate that clonal subpopulations of *P. aeruginosa* cells arrange in vertical striations relative to the gel- or liquid-air interface during macrocolony or pellicle biofilm growth.

135 **Biofilm striations resolve and become longer over time**

The presence of clonal striations in 3-day-old biofilms raised the question of how these features develop over the course of the incubation. To examine this, we grew replicate mixing-assay biofilms and sacrificed the biofilms for microscopic analysis at a series of time points. Fluorescence imaging showed that PA14 cells in macrocolony biofilms are randomly oriented
140 and distributed at 6 and 12 hours of incubation (**Figure 1C**). At 24 hours of incubation the upper two-thirds of the biofilm begin to show clustering and increased vertical orientation of fluorescent cells that gradually becomes more resolved over time. Between 24 and 72 hours of incubation, both zone 1 and zone 2 showed gradual increases in height (3-fold and 2.6-fold, respectively). These observations suggest that cells in zone 1 are able to move away from each other, while
145 in contrast cells in zone 2 remain positioned end-to-end, after division (**Figure 1C**).

Resource availability affects the organization of cellular-arrangement zones and profiles of metabolic activity in biofilms

Biofilms growing at interfaces form resource gradients as they get thicker due to diffusion
150 limitation and consumption by cells closer to the boundary [1,60]. These gradients define chemical microniches that promote physiological differentiation. We hypothesized that changes in resource availability would alter cellular arrangement in *P. aeruginosa* macrocolonies. We tested this assumption by growing mixing-assay biofilms on different concentrations of tryptone and imaging thin-sections by fluorescence microscopy. As expected, biofilms grew thicker
155 when we provided increasing amounts of tryptone, indicating that a vertical tryptone gradient formed across biofilm depth with limiting concentrations at the air interface (**Figure 2B**). We were surprised to find that on 0.25% tryptone fluorescent striations and vertically oriented cells were visible in the zone close to the biofilm base, while dispersed and randomly oriented cells were visible in the upper portion of the biofilm. In contrast, biofilms grown on 0.5% tryptone
160 showed an overall zone organization similar to that seen on 1% tryptone. The ordered region of these biofilms, however, appeared more similar to zone 3 of 1%-tryptone grown biofilms in that cellular orientation showed more deviation from vertical and striations were thicker and not as well-segregated as in biofilms grown on the higher concentration (**Figure 2B**). This further suggests that the level of dispersion displayed by cells in a given zone does not correlate with
165 the absolute concentration of tryptone: for example, the disordered zone corresponded to a tryptone-limited region in the 0.25%-tryptone-grown biofilm, while the disordered zones instead corresponded to the most tryptone-replete regions in the 0.5%- and 1%-tryptone-grown biofilms. These observations show that striation formation is sensitive to nutrient availability but suggest that the absolute concentration of tryptone is not the sole factor determining the organization of
170 cellular-arrangement zones in biofilms.

Because gradients within biofilms affect physiological status, we next sought to test whether the effect of tryptone concentration on cellular-arrangement zone properties and organization correlated with effects on metabolic activity. Our groups have established a protocol to visualize
175 metabolic activity in intact biofilm thin sections using stimulated Raman scattering (SRS) microscopy [40]. In this method, biofilms are grown on agar plates, then transferred to a medium containing D_2O for 24 hours (**Figure 2A**) before the preparation of thin sections. Incorporation of

D into D-C bonds is an indicator of metabolic activity and is detected by SRS microscopy. We found that, for mixing-assay biofilms grown on each concentration of tryptone, metabolic activity peaked at a depth of 40-70 μm (**Figure 2B**). Microelectrode measurements have shown that *P. aeruginosa* biofilms grown at gel-air interfaces contain oxygen gradients [45]. The observation that maximal metabolic activity occurs at a consistent depth in biofilms grown at different tryptone concentrations suggests that maximum metabolic activity occurs where the relative concentrations of oxygen and tryptone are optimized [61]. Strikingly, the region with maximum metabolic activity overlapped with a region containing vertically oriented cells in biofilms grown at all tryptone concentrations (**Figure 2B**).

Global regulators and cell surface components affect cell patterning

P. aeruginosa colony biofilm structure at the macroscale is determined primarily by the regulation of exopolysaccharide production in response to environmental cues and cellular signals [32,33,62–64]. To uncover the genetic determinants of biofilm cellular arrangement at the microscale, we conducted a targeted screen of 48 mutants lacking regulatory proteins, cell surface components, and other factors that contribute to WT biofilm formation and physiology in macrocolonies and other biofilm models (**Figure 3A**) [63–66]. For each of these mutants, a corresponding, constitutively fluorescent strain was generated that expressed the $P_{A1/04/03}$-*mScarlet* construct in the mutant background. Mixed biofilms of each mutant were grown for three days and thin sections were prepared for microscopic analysis.

Imaging allowed us to identify four classes of cellular arrangement phenotypes, which we refer to as “striated”, “bundled”, “disordered”, or “clustered” (**Figure 3B**). Thirty-seven out of the 48 screened mutants showed the “striated” cell arrangement phenotype of the WT (**Figure 3A, B**). Interestingly this class contains several categories of mutants that show altered biofilm development in diverse models [63,67]. These include mutants with altered levels of second messengers; those with defects in primary metabolism; those with deletions of oxygen-sensing or NO-sensing proteins; and those with defects in the production of flagellar components, fimbriae, Pel polysaccharide, or selected virulence factors. This finding shows that effects on biofilm formation and development at the macroscale do not correlate with effects on cellular arrangement at the microscale and across depth.

The remaining 11 mutants showed cellular arrangement phenotypes that differed from the WT. The “bundled” phenotype was observed in all tested genetic knockouts defective in the production and function of the pilus (i.e., *pil* gene mutants and the mutant lacking RpoN, which is required for *pilA* expression) [68,69] (**Figure 3A, B** and **Figure S1**). In this phenotype, the pattern of cellular orientation is similar to that observed for the WT, but striations appear to be bundled because the fluorescently labeled populations are wider and show broader spacing between each other than WT striations. We hypothesize that pilus-mediated motility, known as twitching, serves to distribute cells in the x-y plane before vertical growth in zone 2 promotes the formation of segregated striations in the WT. According to this model, bundled striations form in twitching-defective mutants because daughter cells are less able to move away from their relatives before the elongation of zone 2.

Biofilms with the “disordered” phenotype display a “zone 1”-type distribution of cells across their full depth, i.e. cells are evenly spaced and randomly oriented (**Figure 3B**, **Figures S1** and **S3A**). This was observed in mutants with disruptions in the GacS/GacA two-component system or LasR, both of which constitute regulators that affect the expression of hundreds of genes. In addition, deletion of the O-antigen biosynthetic gene *wbpM* gave rise to this phenotype (**Figure 3B**). O-antigen is the outermost portion of lipopolysaccharide (LPS), a major constituent of the outer membrane of Gram-negative bacteria [70] (**Figure 5A**). The appearance of these biofilms suggests that in these mutants, related cells are fully dispersed from each other. Finally, Δ*ssg* and Δ*wapR*–mutants that are predicted to form LPS without the O-antigen attached (**Figure 3B** and **Figure S1**) [71–73]--gave rise to a “clustered” phenotype. These biofilms showed random cell orientation, but fluorescent cells also formed clusters with vertical elongation in zones 2 and 3, indicating that these mutants retained some ability to arrange related cells along the y-axis (**Figure 3B** and **Figure S1**). We note that our screen did not yield any mutants that exhibit vertical cellular orientation without clustering of related cells (or striation formation). This may indicate that, in zone 2, dispersion after cell division overrides any ability to establish vertical orientation.

A retractable pilus is required for WT cellular arrangement across biofilm depth

To gain further insight into the structure of the bundled phenotype, which arises in mutants with pilus-related defects (**Figure 3A, B** and **4A**), we used high-resolution light sheet microscopy to take top-view images. For this method, the medium was inoculated using a cell suspension containing the $P_{PA1/04/03}$-mScarlet strain at 1% and nonfluorescent cells at 99%. Macrocolonies were imaged after 19 hours of growth. The WT and Δ*pilA* biofilms showed patterns of fluorescence consistent with the distribution of fluorescent cells we observe in biofilm thin-sections taken between 12 and 24 hours (**Figures 1C** and **3D**): striations appears as puncta or as vertical columns that are tilted at an angle away from perfect perpendicularity with the biofilm-air interface. Fluorescent striations in the Δ*pilA* biofilms are thicker and occur at greater distances away from each other than those in WT biofilms. In Δ*pilA*, the striations also generally show a vertical orientation in the biofilm center, but diagonal orientations that radiate toward the colony edge in the biofilm outgrowth (**Figure 4A**). This arrangement is reminiscent of the “hedgehog”-like cellular ordering that has been reported for *Vibrio cholerae* biofilms grown from single cells under flow [12,14].

The phenotypes of the individual *pil* mutants allow us to make inferences about the contributions of the pilus and twitching motility–to cellular arrangement in WT biofilms. Twitching motility is conferred via repeated pilus extension, attachment, and retraction. The primary constituent of the pilus is PilA, also known as pilin. PilB is the extension motor–responsible for pilus assembly–while PilTU is the retraction motor [74,75]. PilO and PilY1 are also both required for pilus assembly; moreover, recent studies have revealed roles for both PilY1 and PilT in surface sensing [76–78]. All of the *pil* mutants we tested show bundled striations in zone 2 highlighting that a functional, i.e., retractable pilus is required for the formation of wild-type striations (**Figure 4B** and **S1**); however, Δ*pilTU* is unique in that it also shows bundled striations in zone 1 (**Figure 4B**).

PilA is required for the zone-2 dispersion observed in O-antigen synthesis and attachment mutants

The results of our screen provide clues regarding the molecular determinants of cellular arrangement in *P. aeruginosa* macrocolonies. First, they suggest that a functional pilus is required for cellular distribution specifically and immediately before the formation of zones 2/3, i.e. that related cells twitch away from each other before they divide and form vertical lineages. However, the pilus is not required for cellular dispersion in zone 1, vertical striation formation, or vertical orientation (**Figure 3B** and **4A, B**). Second, they suggest that modifications to the structure of LPS can affect both cellular orientation and the clustering of related cells (or striation formation). These inferences raise the question of whether these cell surface components show interactions at the regulatory or phenotypic level. We tested this by evaluating PilA protein levels in O-antigen synthesis/attachment mutants and by examining cellular arrangement in combinatorial mutants.

To assess the effect of the LPS mutants on cellular PilA levels, we grew them as macrocolony biofilms for three days before sample preparation. PilA levels were comparable in all tested strains, WT, Δ*wbpM*, Δ*wapR*, and Δ*ssg*, indicating that the distinct cell-arrangement phenotypes are not due to differences in total PilA levels (**Figure 5B**).

To examine phenotypic interactions between mutations that affect O-antigen synthesis/attachment and that which affects pilin production, we created double mutants lacking combinations of the genes *wbpM*, *ssg*, and *pilA*, both with and without the $P_{A1/04/03}$-*mScarlet* construct. Macrocolony biofilm mixing assays revealed that Δ*wbpM* is epistatic on Δ*ssg* (**Figure S1**). This indicates that the presence of O-antigen that is not attached to LPS in Δ*ssg* is sufficient to promote the clustering of related cells observed in this single-gene mutant. Intriguingly, they also revealed that Δ*pilA* is epistatic on Δ*wbpM* and Δ*ssg*: deleting *pilA* in these backgrounds restored the formation of (bundled) striations (**Figure 5C**). These observations suggest that *pilA* promotes dispersion in both the striated WT and non-striated mutants, such as Δ*ssg* and Δ*wbpM*. In the absence of O-antigen-modified LPS, *pilA* also appears to promote random cellular orientation. This finding highlights the intricate interplay between pilus function, O-antigen synthesis/attachment, and cellular organization in the construction of *P. aeruginosa* biofilms. Interestingly, although it remains unconfirmed in *P. aeruginosa* PA14, pilus glycosylation with O-antigen has been described in other *P. aeruginosa* strains [79]. In this context it is also noteworthy that LPS-dependent changes in hydrophobicity have been shown to correlate with altered cellular packing in *P. aeruginosa* aggregates [80].

Cell patterning influences the distribution of substrates across biofilm depth

The distribution of resources throughout a biofilm can be affected by a variety of factors, including its physical structure, properties of the matrix, and the metabolic activity of the cells within [21,81]. To examine whether cellular arrangement impacts how a substrate is distributed within *P. aeruginosa* macrocolonies, we engineered our strains of interest to contain a *rhaSR-PrhaBAD* inducible promoter system designed to express *mScarlet* in response to the small molecule L-rhamnose [82] (**Figure 6C**). Corresponding strains that constitutively produce eGFP were made so that related-cell distribution and rhamnose-induced expression could be

310 examined in the same thin section. Macrocolony biofilms were grown from inocula that contained the constitutive eGFP-producing strain at 2.5% and the RhaSR-*PrhaBAD*-controlled mScarlet-producing strain at 97.5%. These were incubated for three days on our standard medium, then transferred to medium containing L-rhamnose for five hours before they were embedded in paraffin and prepared for thin sectioning (**Figure 6A**). Using this system, we found
315 that in zones 1 and 2 mScarlet production was undetectable or only slightly above that observed in uninduced controls for all strains, indicating that pleiotropic effects inhibited activity of the *rhaSR-PrhaBAD* inducible promoter system in this part of the biofilm. However, all strains showed production of mScarlet in zone 3, i.e. at the biofilm-air interface. We will therefore focus our interpretations only on zone 3. WT, Δ*pilA,* and Δ*pilA*Δ*wbpM* biofilms showed similar,
320 moderate levels of mScarlet production in this region. In the two disordered mutants Δ*wbpM* and Δ*gacA* (**Figure 6B, D** and **Figure S2**), mScarlet production in this region was greatly enhanced. We note that deletion of *wbpM* is not expected to independently affect *PrhaBAD* activity [83]. These findings suggest that lengthwise cellular packing and/or vertical cellular orientation affect the transport of nutrients across biofilm depth.
325

To further examine the effect of cellular arrangement on transport within biofilms, we tested the uptake and distribution of fluorescent microspheres (diameter: 200 nm). Microspheres were spread on the surface of an agar plate before inoculation for macrocolony biofilm growth. After a three-day incubation, the biofilms were imaged from the top or cryosectioned and imaged
330 immediately (**Figure 6E, G**). The microspheres were visible at the air-exposed surface of WT and Δ*wbpM* biofilms. However, in the absence of type IV pili (ΔpilA and ΔpilA ΔwbpM) the microspheres were barely able to pass through to the biofilm surface (**Figure 6F**), indicating pilus-dependent changes in cellular arrangement. To probe the distribution of microspheres within biofilms, we cryosectioned the WT (spheres visible at the surface) and the Δ*pilA* mutant
335 (spheres not visible at the surface). Indeed, microspheres were evenly distributed within WT biofilms, while for Δ*pilA* they were barely able to enter the biofilm at the agar interface (**Figure 6H**). In summary, the distribution of substrates of different sizes (rhamnose and microspheres)--into and within biofilms–was affected by changes in cell arrangement.

340 **Altered cellular arrangement phenotypes correlate with effects on the distributions of metabolically active and surviving cells**

The correlations we observed between cellular-arrangement phenotypes (**Figure 3B**), metabolic activity profiles (**Figure 2B**), and substrate distribution (**Figure 6B, F, H and Figure S2**) in biofilms suggested that mutations that affect microorganization across depth could affect
345 physiological patterning. We therefore tested whether mutant biofilms with altered cellular arrangement show altered distributions of metabolic activity (**Figure 7A**). SRS imaging of mutant biofilm thin-sections indeed revealed that the band of metabolic activity is shifted closer to the top of the biofilm in Δ*wbpM* (peak “2”) when compared to WT (peak “3”) and is unchanged in the Δ*pilA* mutant. The metabolic activity profile of Δ*wbpM* also shows a “shoulder”
350 of increased activity (peak “1”) that is not present in the WT and Δ*pilA*. A double deletion of *wbpM* and *pilA* lacked this shoulder (**Figure 7B**).

To further interrogate physiological status, we assessed cell death across depth in biofilms by exposing them to propidium iodide (PI), a DNA stain that is excluded from bacteria with intact membranes. For this assay, three-day-old biofilms were transferred to plates containing medium supplemented with 50 μM propidium iodide, and incubated for five hours before sample preparation and thin-sectioning (**Figure 7C**). Microscopic imaging revealed increased PI staining in thin sections of Δ*wbpM* biofilms, particularly in the upper region of the biofilm, when compared to WT. Thin sections of WT and Δ*pilA* biofilms showed similar levels and distributions of PI staining (**Figure 7D**).

Together, the results of our metabolic activity and cellular survival profiling experiments are consistent with the notion that more substrates from the growth medium reach the biofilm region at the air interface in the Δ*wbpM* mutant. The altered cellular arrangement in the Δ*wbpM* mutant biofilm appears to disrupt the normal stratification of metabolic activity, pushing it closer to the biofilm surface (**Figure 7B**). The increased PI staining in this region could be a consequence of this accelerated metabolic activity, leading to quicker exhaustion of local resources and, thus, a higher incidence of non-viable cells.

Altered cellular-arrangement patterns correlate with decreased antibiotic tolerance

The physiological status of a bacterium affects its susceptibility to antibiotics, and particularly those that target biosynthetic reactions and/or that require functional membrane transport processes for uptake [84–87]. Because we had observed that mutants with altered cellular arrangements showed distinct patterns of substrate distribution and metabolic activity within biofilms (**Figure 6B, F, H, Figure 7B, and Figure S2**), we hypothesized that they would be differentially susceptible to antibiotic treatment. To test this, we transferred three-day-old *P. aeruginosa* macrocolonies to a medium containing propidium iodide and tobramycin, an aminoglycoside antibiotic that requires proton motive force for its bactericidal action, and incubated for five hours before biofilms were prepared for thin-sectioning [88]. We infer that an increase in propidium iodide staining indicates a decrease in antibiotic tolerance [89,90]. Comparison to thin-sections from biofilms that had not been treated with tobramycin (**Figure 7D**) revealed that, in WT and Δ*pilA*, the antibiotic killed cells in the region spanning from 20-60 μm from the air-biofilm interface, which corresponded to the regions of high metabolic activity (**Figure 7B**). In contrast, Δ*wbpM* and Δ*gacA* biofilm thin-sections showed tobramycin-dependent cell death in a region that was closer to the air-biofilm interface (0-40 μm depth) (**Figure 7D, Figure S3B, S3C**), corresponding to the shifted region of high metabolic activity that we had observed for Δ*wbpM* (**Figure 7B**). In agreement with the dominant effect of the *pilA* deletion on cell arrangement (**Figure 5C** and **Figure S3A**) and metabolic activity (**Figure 7B**), the peak of propidium iodide staining shifted back to a depth of 20-60 μm in the Δ*gacA*Δ*pilA* double mutant (**Figure S3C**). While cells are randomly oriented in Δ*wbpM* and Δ*gacA* biofilms, the deletion of *pilA* in these backgrounds results in vertical cellular arrangement as observed in WT and Δ*pilA* (**Figure 5C** and **Figure S3A**)**.** These patterns further highlight the correlation between cellular arrangement and antibiotic tolerance.

Because our data suggest that cellular arrangement affects substrate transport across biofilm depth, two phenomena may be contributing to the differential impact of tobramycin treatment on

ordered (WT) and disordered-mutant biofilms. First, tobramycin, like rhamnose, may move more readily through disordered biofilms than through ordered ones, leading to a shift in the zone of tobramycin-dependent cell death toward the biofilm-air interface. Alternatively or in addition, the greater availability of rhamnose near the biofilm-air interface in disordered mutants like Δ*wbpM*– which appears to enhance metabolic activity in this zone–may also contribute to tobramycin susceptibility. Regardless of whether one or both of these phenomena are responsible for changes in the disordered-mutant profiles, our data indicate a relationship between cellular organization and the physiological properties of the biofilm that impacts antibiotic tolerance.

Concluding remarks

This study has uncovered genetic and structural determinants that orchestrate cell arrangement within *P. aeruginosa* biofilms. A screen of 48 mutants representing genes implicated in biofilm development and physiology identified 11 that impact cellular organization across depth, underscoring that this aspect of biofilm architecture is uniquely controlled. Our work also revealed correlations between cellular arrangement phenotypes and impacts on substrate distribution, metabolic activity, and antibiotic tolerance highlighting the critical role of microorganization in determining metabolic status. An understanding of the relationships between microanatomy and physiology, not only deepens our knowledge of bacterial multicellularity and provides avenues for the development of new therapeutic strategies. It also prompts further exploration into the potential parallels and divergences between biofilm mechanisms and multicellular organization in other organisms, paving the way for interdisciplinary insights.

MATERIALS AND METHODS

Bacterial strains and culture conditions

Bacterial strains used in this study are listed in Table 1. Liquid cultures were routinely grown in
425 Lysogeny Broth (LB) [91] at 37 ˚C with shaking at 250 rpm.

Construction of mutant *P. aeruginosa* strains

To create markerless deletion mutants in *P. aeruginosa* PA14, 1 kb of flanking sequence from each side of the target gene were amplified using the primers listed in Table 3 and inserted into
430 pMQ30 through gap repair cloning in Saccharomyces cerevisiae InvSc1 [92]. Each plasmid listed in Table 2 was transformed into Escherichia coli strain UQ950, verified by sanger sequencing, and moved into PA14 using biparental conjugation. PA14 single recombinants were selected on LB agar plates containing 100 µg/ml gentamicin. Double recombinants (markerless deletions) were selected on LB without NaCl and modified to contain 10% sucrose.
435 Genotypes of deletion mutants were confirmed by PCR. Combinatorial mutants were constructed by using single mutants as hosts for biparental conjugation.

Scanning electron microscopy of macrocolonies

Overnight precultures were diluted 1:100 in LB and grown to mid-exponential phase (OD at 500
440 nm ~ 0.5). OD values at 500 nm were read in a Spectronic 20D+ spectrophotometer (Thermo Fisher Scientific [Waltham, MA]) and cultures were adjusted to the same OD. Five microliters of mixture were spotted onto a bilayer plate. After three days of incubation, macrocolonies were carefully overlaid with 1% agar to preserve their structure. Blocks were then cut out, and the bottom layer of the agar was carefully removed, leaving an equal volume on top and below the
445 macrocolony. The blocks were then placed on filter paper to facilitate moving them when necessary with the least amount of disturbance and placed into an empty glass petri dish. The blocks were then incubated in McDowell Trump Fixative for 16 hours at room temperature to allow fixation to occur. They were washed twice with 0.1 M PBS before being subjected to 1% (wt/vol) Osmium Tetroxide in 0.1 M PBS to further fix the samples. The samples were then
450 washed twice with distilled water before being subjected to dehydration in an increasing graded ethahol series (35%, 50%, 75%, 2X 90%, 3X 100%). The blocks were washed twice in HMDS before being mounted onto aluminum stubs using double-sided round carbon stickers and placed into a dessicator. After air-drying thoroughly, the blocks were cut in half in order to visualize the internal structure and orientation of cells within the biofilm. The samples were then
455 coated in gold using a Leica EM ACE600 Coater. The samples were visualized using an Helios Nanolab DualBeam 660 (FEI) operating at an accelerating voltage of 5 kV under a high vacuum.

Colony biofilm mixing assay

Overnight precultures were diluted 1:100 in LB and grown to mid-exponential phase (OD at 500
460 nm ~ 0.5). OD values at 500 nm values were read in a Spectronic 20D+ spectrophotometer (Thermo Fisher Scientific [Waltham, MA]) and cultures were adjusted to the same OD. Adjusted cultures were then mixed in a 2.5:97.5 ratio of fluorescent:non-fluorescent cells. Five microliters of mixture were spotted onto a bilayer plate of 45 mL (bottom layer) and 15mL (top layer) of 1% tryptone, 1% agar [Teknova (Hollister, CA) A7777] in a 10 cm x 10 cm x 1.5 cm square Petri

465 dish (LDP [Wayne, NJ] D210-16). Plates were incubated for three days at 25˚C in the dark and imaged using a VHX-1000 digital microscope (Keyence, Japan).

Paraffin embedding, thin sectioning and confocal imaging

After three days of growth as described above, biofilms were overlaid with 1% agar and
470 sandwiched biofilms were lifted from the bottom layer and fixed overnight in 4% paraformaldehyde in PBS at 25 °C for 24 h in the dark. Fixed biofilms were washed twice in PBS and dehydrated through a series of 60-min ethanol washes (25%, 50%, 70%, 95%, 3 × 100% ethanol) and cleared via three 60-min incubations in Histoclear-II (National Diagnostics); these steps were performed using an STP120 Tissue Processor (Thermo Fisher Scientific).
475 Biofilms were then infiltrated with wax via two separate 2-h washes of 100% paraffin wax (Paraplast Xtra) at 55 °C, and allowed to polymerize overnight at 4 °C. Trimmed blocks were sectioned in 10-μm-thick sections perpendicular to the plane of the biofilm, floated onto water at 42 °C, and collected onto slides. Slides were air-dried overnight, heat-fixed on a hotplate for 30 minutes at 45 °C, and rehydrated in the reverse order of processing. Rehydrated colonies were
480 immediately mounted in (Thermo Fisher Scientific ProLong™ Diamond Antifade Mountant P36965) and overlaid with a coverslip. Fluorescent images were captured using an LSM800 confocal microscope (Zeiss, Germany). Samples were illuminated with 488 and 561 nm lasers, respectively. eGFP acquisition parameters were: 400-548nm (emission wavelength range). mScarlet acquisition parameters were: 593-700nm (emission wavelength range). Each strain
485 was prepared in this manner in at least biological triplicates.

Image analysis and quantification of biofilm microorganization

Image analysis was performed in FIJI [93] and Python (Python Software Foundation; Python Language Reference, version 3.8. Available at www.python.org). Each image was viewed in
490 FIJI for quality control and then binarized using a custom Python script. For each sample, a fixed-threshold binarization was applied to the fluorescence image using a multi-level version of Otsu's method, which separates pixels of an input image into several classes obtained according to intensity [94]. For most images, the number of classes *n* was set to three, and the image was binarized by setting pixels in the brightest class equal to one and all others to zero.
495 Qualitative inspection of the thresholded images were performed for quality assurance; samples which yielded poor separation into three classes (due to, e.g., lower resolution or fluorescence intensity) were binarized using the classic Otsu's method [95]. Images were then cleaned by using masks to remove artifacts. All successive analysis and quantification was performed using the cleaned binarized images.
500

Boundaries of individual cells were segmented from binarized images using the Python SciPy package [96]. The orientation of each cell was determined as the angle between the horizontal and the major axis of the best-fit ellipse to each cell, ranging from -90 to +90 degrees. Heights along the biofilm's direction of growth were divided into bins of 25 pixels in width. An order
505 parameter to quantify cell alignment was defined as the standard deviation of the orientation of all cells within a bin; a high value indicates that cells in a bin are randomly oriented, while a low value indicates that cells are aligned in the same direction. All code is available at https://github.com/jnirody/biofilms.

510 **Pellicle biofilm mixing assay**

Overnight precultures of fluorescent (mScarlet-expressing) and non-fluorescent strains were diluted 1:100 in LB and grown to mid-exponential phase (OD at 500 nm ~ 0.5). OD values at 500 nm values were read in a Spectronic 20D+ spectrophotometer (Thermo Fisher Scientific [Waltham, MA]) and cultures were adjusted to the same OD. Adjusted cultures were then mixed
515 in a 2.5:97.5 ratio of fluorescent:non-fluorescent cells and nine ml of this mixture was added to 13x100mm culture tubes (VWR, Cat no. 10545-936) and grown in 25˚C incubator for three days. Pellicles were removed from glass tube using a sterile needle and transferred to plate and overlayed with 1% agar. Samples were subsequently processed using standard paraffin embedding and thin sectioning protocol.

520

Stimulated Raman Scattering Microscopy

Five microliters of a bacterial subculture were spotted onto 45mL/15mL two-layer 1% tryptone 1% agar plates and were grown for 72 hours, then the top layer and biofilm was transferred to 2 mL 1% tryptone 1% agar 50% D_2O and incubated at 25°C for 5 hours or 24 hours. The biofilms
525 were then thin sectioned as described above. For SRS microscopy, an integrated laser source (picoEMERALD, Applied Physics & Electronics, Inc.) was used to produce both a Stokes beam (1064nm, 6ps, intensity modulated at 8MHz) and a tunable pump beam (720–990nm, 5–6ps) at an 80MHz repetition rate. The spectral resolution of SRS is FWHM=6–7cm^{-1}. These two spatially and temporally overlapped beams with optimized near-IR throughput were coupled into
530 an inverted multiphoton laser-scanning microscope (FV1200MPE, Olympus). Both beams were focused on the biofilm samples through a 25X water objective (XLPlan N, 1.05 N.A. MP, Olympus) and collected with a high N.A. oil condenser lens (1.4 N.A., Olympus) after the sample. By removing the Stokes beam with a high O.D. bandpass filter (890/220 CARS, Chroma Technology), the pump beam is detected with a large area Si photodiode (FDS1010,
535 Thorlabs) reverse-biased by 64 DC voltage. The output current of the photodiode was electronically filtered (KR 2724, KR electronics), terminated with 50Ω, and demodulated with a lock-in amplifier (HF2LI, Zurich Instruments) to achieve near shot-noise-limited sensitivity. The stimulated Raman loss signal at each pixel was sent to the analog interface box (FV10-ANALOG, Olympus) of the microscope to generate the image. All images were acquired with 80
540 μs time constant at the lock-in amplifier and 100μs pixel dwell time (~27s per frame of 512×512 pixels). Measured after the objectives, 40mW pump power and 120mW Stokes beam were used to image the carbon-deuterium 2183 cm^{-1} and off-resonance 2004 cm^{-1} channels.

Macrocolony clearing and light sheet microscopy

545 Overnight precultures were diluted 1:100 in LB and grown to mid-exponential phase (OD at 500 nm ~ 0.5). OD values at 500 nm values were read in a Spectronic 20D+ spectrophotometer (Thermo Fisher Scientific [Waltham, MA]) and cultures were adjusted to the same OD. Adjusted cultures were then mixed in a 1:100 ratio of fluorescent:non-fluorescent cells. 0.5 microliters of mixture were spotted onto a bilayer plate of 50 mL (bottom layer) and 10 mL (top layer) of 1%
550 tryptone, 1% agar [Teknova (Hollister, CA) A7777] in a 10 cm x 10 cm x 1.5 cm square Petri dish (LDP [Wayne, NJ] D210-16). Plates were incubated for one day at 25˚C in the dark. Biofilms were overlaid with 1% agar, and sandwiched biofilms were lifted from the bottom layer,

and fixed overnight in 4% paraformaldehyde in PBS at 25 °C for 12 hours in the dark. Fixed biofilms were washed twice in PBS then incubated for three hours in 70% (V/V) glycerol solution deionized water solution for optical clearing. The clarified biofilms were mounted on a standard microscopy slide, and were imaged with ClearScope [97] (MBF Biosciences) light sheet microscope, using Nikon 20x/1.0NA detection objective. The resulting image tiles were stitched by using a Terastitcher based custom pipeline [98,99], and analyzed using ImageJ after 2-fold down-sampling in x-y axes.

SDS-page and western

Sheared pilin and cell lysate proteins were extracted as previously described [100] with some modifications. Overnight precultures were diluted 1:100 in LB and grown to mid-exponential phase (OD at 500 nm ~ 0.5). OD values at 500 nm values were read in a Spectronic 20D+ spectrophotometer (Thermo Fisher Scientific [Waltham, MA]) and cultures were adjusted to the same OD. Five microliters of mixture were spotted onto a plate of 60 mL of 1% tryptone, 1% agar [Teknova (Hollister, CA) A7777] in a 10 cm x 10 cm x 1.5 cm square Petri dish (LDP [Wayne, NJ] D210-16). Plates were incubated for three days at 25˚C in the dark.

Biofilm samples (25 biofilms per strain) were gently scraped from agar, resuspended in 1 mL sterile PBS (phosphate buffered saline, pH 7.4), and centrifuged at 4000 x g for five minutes at room temperature. Pellets were resuspended in 4.5 mL of sterile PBS, vortexed for 30 s to shear cell surface proteins, and centrifuged at 4000 x g for 15 min at room temperature. Supernatants containing the sheared surface proteins were subjected to multiple rounds of centrifugation at 11,600 x g for 15 min to remove residual cells from the samples. Next, 5 M NaCl and 30% (w/v) PEG (polyethylene glycol, ~8000 MW, Sigma) at a volume ratio of 0.1 each were added to the total supernatant, and incubated on ice for 90 min before pilin was collected by centrifugation at 11,600 x g for 30 min at 4 °C. The pelleted pilin was resuspended in 1X LDS sample buffer (Invitrogen) with 5% β-mercaptoethanol (Sigma) and boiled for 5 min before separation on a 4-12% NuPAGE Bis-Tris gel (Invitrogen) for immunoblotting.

Cellular proteins were extracted from the cell pellets after surface pilin was sheared and removed (described above). Briefly, cell pellets were resuspended in 0.2 M Tris-Cl (pH 8.0), normalized to OD_{600} ~ 4.0, centrifuged, and pellets were resuspended in 1X LDS sample buffer with 5% β-mercaptoethanol. Samples were boiled for five min, centrifuged, and aliquots from the supernatants were resolved on a 4-12% NuPAGE Bis-Tris gel for visualization and immunoblotting.

For PilA immunoblotting, both sheared and whole-cell pilin preparations were resolved using 4-12% NuPAGE Bis-Tris gels at 125V for 2.5 h and transferred onto 0.22 µm nitrocellulose membranes. Protein bands were normalized to total protein visualized by BLOT-FastStain (GBiosciences). Membranes were blocked using TBS-T (Tris-buffered saline with Tween-20) containing 5% milk before probing with an anti-PilA rabbit polyclonal antibody (gift of the O'Toole lab, Dartmouth) at 1:1000, followed by an IR conjugated goat anti-rabbit antibody at 1:10,000 (LI-COR Biosciences). Bands were visualized using the LI-COR Odyssey Clx imager and Image Studio.

Rhamnose assay

Overnight precultures were diluted 1:100 in LB and grown to mid-exponential phase (OD at 500 nm ~ 0.5). OD values at 500 nm values were read in a Spectronic 20D+ spectrophotometer (Thermo Fisher Scientific [Waltham, MA]) and cultures were adjusted to the same OD. Adjusted cultures were then mixed in a 2.5:97.5 ratio of constitutively fluorescent eGFP cells : rhamnose inducible mScarlet fluorescent cells. Five microliters of mixture were spotted onto bilayer plater. Plates were incubated for three days at 25 ˚C in the dark, then transferred to medium containing 0.5% L-rhamnose for five hours. Samples were subsequently processed using standard paraffin embedding and thin sectioning protocol.

Microsphere assay

Overnight precultures were diluted 1:100 in LB and grown to mid-exponential phase (OD at 500 nm ~ 0.5). OD values at 500 nm values were read in a Spectronic 20D+ spectrophotometer (Thermo Fisher Scientific [Waltham, MA]) and cultures were adjusted to the same OD. Adjusted cultures were then mixed in a 2.5:97.5 ratio of fluorescent:non-fluorescent cells. Bilayer plates of 45 mL (bottom layer) and 15 mL (top layer) of 1% tryptone, 1% agar [Teknova (Hollister, CA) A7777] in a 10 cm x 10 cm x 1.5 cm square Petri dish (LDP [Wayne, NJ] D210-16) were made and solidified overnight. 300 µl (10^10 microspheres/mL) of Fluoresbrite® Multifluorescent Microspheres 0.2 µm (PolySciences 24050-5) were spread onto a bilayer plate using sterile glass beads and dried for 30 minutes. Five microliters of bacterial culture mixture were spotted onto plate and incubated for three days at 25 ˚C in the dark and macrocolony biofilms were subsequently imaged live or prepared for cryosectioning. Samples were imaged on a ZEISS Axio Zoom.V16 microscope, equipped with a mercury lamp. eGFP was detected using a 450/490nm excitation filter, 500/550nm emission filter, and 495nm dichroic mirror. Fluoresbrite® Multifluorescent Microspheres were detected using a 538/562nm excitation filter, 570/640nm emission filter, and 570nm dichroic mirror.

Macrocolony biofilm cryosectioning

Macrocolony biofilms were overlaid with 1% agar, and sandwiched biofilms were cut and lifted from the bottom layer, and placed in disposable cryomold (Tissue-Tek). They were then covered with an embedding agent (Tissue-Tek OCT), and flash frozen in liquid nitrogen. Cryoembedded biofilms were subsequently sectioned with a Leica CM1950 cryostat set at −18 °C. Ten-micrometer-thick sections perpendicular to the plane of the macrocolony were then transferred onto slides and immediately imaged using a ZEISS Axio Zoom.V16.

Propidium iodide and antibiotic assay

Overnight precultures were diluted 1:100 in LB and grown to mid-exponential phase (OD at 500 nm ~ 0.5). OD values at 500 nm were read in a Spectronic 20D+ spectrophotometer (Thermo Fisher Scientific [Waltham, MA]) and cultures were adjusted to the same OD. Adjusted cultures were then mixed in a 2.5:97.5 ratio of eGFP fluorescent:non-fluorescent cells. Five microliters of mixture were spotted onto bilayer plate. Plates were incubated for three days at 25 ˚C in the dark, then transferred to medium containing 50 µM PI with and without 100 µg/mL tobramycin for five hours. Samples were subsequently processed using standard paraffin embedding and

thin sectioning protocol. Samples were imaged on a ZEISS Axio Zoom.V16 microscope, equipped with a mercury lamp. Propidium iodide staining was detected using a 538/562nm excitation filter, 570/640nm emission filter, and 570nm dichroic mirror.

ACKNOWLEDGEMENTS

The authors thank Endah Rosa, Paula Fernandez Musso and Yu-Cheng Lin for assistance in generating mutants described in this manuscript. Thank you to the O'Toole Lab for gifting the anti-PilA rabbit polyclonal antibody. This work was supported by an NIH Diversity supplement to J.K. and by the parent NIH/NIAID grant, R01AI103369 to L.E.P.D. It was also supported by National Institute of Health (R01 EB029523) and Chan Zuckerberg Initiative (Dynamic Imaging 2023-321166) to W.M., a Rockefeller University Physics and Biology Fellowship and an All Souls College Fellowship in Life Sciences to J.A.N., NSF MCB 2216676 funding to A.J., and NIH DP2MH119423 and 1R44MH116827 funding to R.T.

REFERENCES

1. Jo J, Price-Whelan A, Dietrich LEP. Gradients and consequences of heterogeneity in biofilms. Nat Rev Microbiol. 2022;20: 593–607.

2. Azimi S, Lewin GR, Whiteley M. The biogeography of infection revisited. Nat Rev Microbiol. 2022;20: 579–592.

3. Hall-Stoodley L, Costerton JW, Stoodley P. Bacterial biofilms: from the natural environment to infectious diseases. Nat Rev Microbiol. 2004;2: 95–108.

4. O'Toole G, Kaplan HB, Kolter R. Biofilm formation as microbial development. Annu Rev Microbiol. 2000;54: 49–79.

5. Mah TF, O'Toole GA. Mechanisms of biofilm resistance to antimicrobial agents. Trends Microbiol. 2001;9: 34–39.

6. Costerton JW, Stewart PS, Greenberg EP. Bacterial biofilms: a common cause of persistent infections. Science. 1999;284: 1318–1322.

7. Alberts B, Johnson A, Lewis J, Raff M, Roberts K, Walter P. Molecular Biology of the Cell. 2002 [cited 28 Mar 2023]. Available: https://www.ncbi.nlm.nih.gov/books/NBK21054/

8. Flemming H-C, Wingender J, Szewzyk U, Steinberg P, Rice SA, Kjelleberg S. Biofilms: an emergent form of bacterial life. Nat Rev Microbiol. 2016;14: 563–575.

9. Shrout JD, Tolker-Nielsen T, Givskov M, Parsek MR. The contribution of cell-cell signaling and motility to bacterial biofilm formation. MRS Bull. 2011;36: 367–373.

10. Nadell CD, Drescher K, Foster KR. Spatial structure, cooperation and competition in biofilms. Nat Rev Microbiol. 2016;14: 589–600.

11. Yaman YI, Demir E, Vetter R, Kocabas A. Emergence of active nematics in chaining bacterial biofilms. Nat Commun. 2019;10: 2285.

12. Drescher K, Dunkel J, Nadell CD, van Teeffelen S, Grnja I, Wingreen NS, et al. Architectural transitions in Vibrio cholerae biofilms at single-cell resolution. Proc Natl Acad Sci U S A. 2016;113: E2066–72.

13. Serra DO, Richter AM, Hengge R. Cellulose as an architectural element in spatially structured Escherichia coli biofilms. J Bacteriol. 2013;195: 5540–5554.

14. Yan J, Sharo AG, Stone HA, Wingreen NS, Bassler BL. *Vibrio cholerae* biofilm growth program and architecture revealed by single-cell live imaging. Proc Natl Acad Sci U S A. 2016;113: E5337–43.

15. Kasetty S, Mould DL, Hogan DA, Nadell CD. Both Pseudomonas aeruginosa and Candida albicans Accumulate Greater Biomass in Dual-Species Biofilms under Flow. mSphere. 2021;6: e0041621.

16. Teschler JK, Nadell CD, Drescher K, Yildiz FH. Mechanisms Underlying Vibrio cholerae Biofilm Formation and Dispersion. Annu Rev Microbiol. 2022;76: 503–532.

17. Barken KB, Pamp SJ, Yang L, Gjermansen M, Bertrand JJ, Klausen M, et al. Roles of type IV pili, flagellum-mediated motility and extracellular DNA in the formation of mature multicellular structures in Pseudomonas aeruginosa biofilms. Environ Microbiol. 2008;10: 2331–2343.

18. Stewart PS, Franklin MJ. Physiological heterogeneity in biofilms. Nat Rev Microbiol. 2008;6: 199–210.

19. Ghanbari A, Dehghany J, Schwebs T, Müsken M, Häussler S, Meyer-Hermann M. Inoculation density and nutrient level determine the formation of mushroom-shaped structures in Pseudomonas aeruginosa biofilms. Sci Rep. 2016;6: 32097.

20. Wilking JN, Zaburdaev V, Volder MD, Losick R, Brenner MP, Weitz DA. Liquid transport facilitated by channels in *Bacillus subtilis* biofilms. Proceedings of the National Academy of Sciences. 2013;110: 848–852.

21. Rooney LM, Amos WB, Hoskisson PA, McConnell G. Intra-colony channels in E. coli function as a nutrient uptake system. ISME J. 2020;14: 2461–2473.

22. Ziege R, Tsirigoni A-M, Large B, Serra DO, Blank KG, Hengge R, et al. Adaptation of Escherichia coli Biofilm Growth, Morphology, and Mechanical Properties to Substrate Water Content. ACS Biomater Sci Eng. 2021;7: 5315–5325.

23. Vlamakis H, Aguilar C, Losick R, Kolter R. Control of cell fate by the formation of an architecturally complex bacterial community. Genes Dev. 2008;22: 945–953.

24. Costerton JW, Lewandowski Z, Caldwell DE, Korber DR, Lappin-Scott HM. Microbial biofilms. Annu Rev Microbiol. 1995;49: 711–745.

25. Rattray J, Walden R, Zacarias PM, Molotkova E, Perron G, Solis-Lemus C, et al. Machine learning identification of Pseudomonas aeruginosa strains from colony image data. bioRxiv. 2022. p. 2022.09.02.506375. doi:10.1101/2022.09.02.506375

26. Pence MA, Liesman R. Chapter 55 - Clinical microbiology. In: Clarke W, Marzinke MA, editors. Contemporary Practice in Clinical Chemistry (Fourth Edition). Academic Press; 2020. pp. 985–1006.

27. Merritt JH, Kadouri DE, O'Toole GA. Growing and analyzing static biofilms. Curr Protoc Microbiol. 2005;Chapter 1: Unit 1B.1.

725 28. Ray VA, Morris AR, Visick KL. A semi-quantitative approach to assess biofilm formation using wrinkled colony development. J Vis Exp. 2012; e4035.

29. Franklin MJ, Nivens DE, Weadge JT, Howell PL. Biosynthesis of the Pseudomonas aeruginosa Extracellular Polysaccharides, Alginate, Pel, and Psl. Front Microbiol. 2011;2: 167.

730 30. O'Toole GA. Microtiter dish biofilm formation assay. J Vis Exp. 2011. doi:10.3791/2437

31. Ramos I, Dietrich LEP, Price-Whelan A, Newman DK. Phenazines affect biofilm formation by Pseudomonas aeruginosa in similar ways at various scales. Res Microbiol. 2010;161: 187–191.

32. Okegbe C, Fields BL, Cole SJ, Beierschmitt C, Morgan CJ, Price-Whelan A, et al. Electron-
735 shuttling antibiotics structure bacterial communities by modulating cellular levels of c-di-GMP. Proc Natl Acad Sci U S A. 2017;114: E5236–E5245.

33. Friedman L, Kolter R. Genes involved in matrix formation in Pseudomonas aeruginosa PA14 biofilms. Mol Microbiol. 2004;51: 675–690.

34. Rakhimova E, Munder A, Wiehlmann L, Bredenbruch F, Tümmler B. Fitness of isogenic
740 colony morphology variants of Pseudomonas aeruginosa in murine airway infection. PLoS One. 2008;3: e1685.

35. Serra DO, Hengge R. Bacterial Multicellularity: The Biology of Escherichia coli Building Large-Scale Biofilm Communities. Annu Rev Microbiol. 2021;75: 269–290.

36. Díaz-Pascual F, Lempp M, Nosho K, Jeckel H, Jo JK, Neuhaus K, et al. Spatial alanine
745 metabolism determines local growth dynamics of Escherichia coli colonies. Elife. 2021;10. doi:10.7554/eLife.70794

37. Klauck G, Serra DO, Possling A, Hengge R. Spatial organization of different sigma factor activities and c-di-GMP signalling within the three-dimensional landscape of a bacterial biofilm. Open Biol. 2018;8. doi:10.1098/rsob.180066

750 38. Williamson KS, Richards LA, Perez-Osorio AC, Pitts B, McInnerney K, Stewart PS, et al. Heterogeneity in Pseudomonas aeruginosa biofilms includes expression of ribosome hibernation factors in the antibiotic-tolerant subpopulation and hypoxia-induced stress response in the metabolically active population. J Bacteriol. 2012;194: 2062–2073.

39. Recinos DA, Sekedat MD, Hernandez A, Cohen TS, Sakhtah H, Prince AS, et al.
755 Redundant phenazine operons in Pseudomonas aeruginosa exhibit environment-dependent expression and differential roles in pathogenicity. Proc Natl Acad Sci U S A. 2012;109: 19420–19425.

40. Schiessl KT, Hu F, Jo J, Nazia SZ, Wang B, Price-Whelan A, et al. Phenazine production

promotes antibiotic tolerance and metabolic heterogeneity in Pseudomonas aeruginosa biofilms. Nat Commun. 2019;10: 762.

41. Madsen JS, Lin Y-C, Squyres GR, Price-Whelan A, de Santiago Torio A, Song A, et al. Facultative control of matrix production optimizes competitive fitness in Pseudomonas aeruginosa PA14 biofilm models. Appl Environ Microbiol. 2015;81: 8414–8426.

42. Cabeen MT, Leiman SA, Losick R. Colony-morphology screening uncovers a role for the Pseudomonas aeruginosa nitrogen-related phosphotransferase system in biofilm formation. Mol Microbiol. 2016;99: 557–570.

43. Ha D-G, Richman ME, O'Toole GA. Deletion mutant library for investigation of functional outputs of cyclic diguanylate metabolism in Pseudomonas aeruginosa PA14. Appl Environ Microbiol. 2014;80: 3384–3393.

44. Arnaouteli S, Ferreira AS, Schor M, Morris RJ, Bromley KM, Jo J, et al. Bifunctionality of a biofilm matrix protein controlled by redox state. Proc Natl Acad Sci U S A. 2017;114: E6184–E6191.

45. Jo J, Cortez KL, Cornell WC, Price-Whelan A, Dietrich LE. An orphan cbb3-type cytochrome oxidase subunit supports Pseudomonas aeruginosa biofilm growth and virulence. Elife. 2017;6. doi:10.7554/eLife.30205

46. Bellin DL, Sakhtah H, Zhang Y, Price-Whelan A, Dietrich LEP, Shepard KL. Electrochemical camera chip for simultaneous imaging of multiple metabolites in biofilms. Nat Commun. 2016;7: 10535.

47. Ciccarese D, Micali G, Borer B, Ruan C, Or D, Johnson DR. Rare and localized events stabilize microbial community composition and patterns of spatial self-organization in a fluctuating environment. ISME J. 2022;16: 1453–1463.

48. Julián E, Roldán M, Sánchez-Chardi A, Astola O, Agustí G, Luquin M. Microscopic cords, a virulence-related characteristic of Mycobacterium tuberculosis, are also present in nonpathogenic mycobacteria. J Bacteriol. 2010;192: 1751–1760.

49. Repula A, Abraham E, Cherpak V, Smalyukh II. Biotropic liquid crystal phase transformations in cellulose-producing bacterial communities. Proc Natl Acad Sci U S A. 2022;119: e2200930119.

50. Nijjer J, Li C, Zhang Q, Lu H, Zhang S, Yan J. Mechanical forces drive a reorientation cascade leading to biofilm self-patterning. Nat Commun. 2021;12: 6632.

51. Cho H, Jönsson H, Campbell K, Melke P, Williams JW, Jedynak B, et al. Self-organization in high-density bacterial colonies: efficient crowd control. PLoS Biol. 2007;5: e302.

52. Volfson D, Cookson S, Hasty J, Tsimring LS. Biomechanical ordering of dense cell

populations. Proc Natl Acad Sci U S A. 2008;105: 15346–15351.

53. Puri D, Fang X, Allison KR. Evidence of a possible multicellular life cycle in Escherichia coli. iScience. 2023;26: 105795.

54. DePas WH, Bergkessel M, Newman DK. Aggregation of Nontuberculous Mycobacteria Is Regulated by Carbon-Nitrogen Balance. MBio. 2019;10. doi:10.1128/mBio.01715-19

55. Mizuno K, Maree M, Nagamura T, Koga A, Hirayama S, Furukawa S, et al. Novel multicellular prokaryote discovered next to an underground stream. Elife. 2022;11. doi:10.7554/eLife.71920

56. Basaran M, Yaman YI, Yüce TC, Vetter R, Kocabas A. Large-scale orientational order in bacterial colonies during inward growth. Elife. 2022;11. doi:10.7554/eLife.72187

57. Cornell WC, Morgan CJ, Koyama L, Sakhtah H, Mansfield JH, Dietrich LEP. Paraffin Embedding and Thin Sectioning of Microbial Colony Biofilms for Microscopic Analysis. J Vis Exp. 2018. doi:10.3791/57196

58. Razvi E, Whitfield GB, Reichhardt C, Dreifus JE, Willis AR, Gluscencova OB, et al. Glycoside hydrolase processing of the Pel polysaccharide alters biofilm biomechanics and Pseudomonas aeruginosa virulence. NPJ Biofilms Microbiomes. 2023;9: 7.

59. Spiers AJ, Bohannon J, Gehrig SM, Rainey PB. Biofilm formation at the air-liquid interface by the Pseudomonas fluorescens SBW25 wrinkly spreader requires an acetylated form of cellulose. Mol Microbiol. 2003;50: 15–27.

60. Werner E, Roe F, Bugnicourt A, Franklin MJ, Heydorn A, Molin S, et al. Stratified Growth in *Pseudomonas aeruginosa* Biofilms. Applied and Environmental Microbiology. 2004. pp. 6188–6196. doi:10.1128/aem.70.10.6188-6196.2004

61. Evans CR, Smiley MK, Thio SA, Wei M, Price-Whelan A, Min W, et al. Spatial heterogeneity in biofilm metabolism elicited by local control of phenazine methylation. bioRxiv. 2023. doi:10.1101/2023.02.15.528762

62. Mukherjee S, Jemielita M, Stergioula V, Tikhonov M, Bassler BL. Photosensing and quorum sensing are integrated to control Pseudomonas aeruginosa collective behaviors. PLoS Biol. 2019;17: e3000579.

63. Ma LZ, Wang D, Liu Y, Zhang Z, Wozniak DJ. Regulation of Biofilm Exopolysaccharide Biosynthesis and Degradation in Pseudomonas aeruginosa. Annu Rev Microbiol. 2022;76: 413–433.

64. Ha D-G, O'Toole GA. c-di-GMP and its Effects on Biofilm Formation and Dispersion: a Pseudomonas Aeruginosa Review. Microbiol Spectr. 2015;3: MB–0003–2014.

65. Hickman JW, Tifrea DF, Harwood CS. A chemosensory system that regulates biofilm formation through modulation of cyclic diguanylate levels. Proc Natl Acad Sci U S A. 2005;102: 14422–14427.

66. Roy AB, Petrova OE, Sauer K. The phosphodiesterase DipA (PA5017) is essential for Pseudomonas aeruginosa biofilm dispersion. J Bacteriol. 2012;194: 2904–2915.

67. Wong GCL, Antani JD, Lele PP, Chen J, Nan B, Kühn MJ, et al. Roadmap on emerging concepts in the physical biology of bacterial biofilms: from surface sensing to community formation. Phys Biol. 2021;18. doi:10.1088/1478-3975/abdc0e

68. Ishimoto KS, Lory S. Formation of pilin in Pseudomonas aeruginosa requires the alternative sigma factor (RpoN) of RNA polymerase. Proc Natl Acad Sci U S A. 1989;86: 1954–1957.

69. Burrows LL. Pseudomonas aeruginosa twitching motility: type IV pili in action. Annu Rev Microbiol. 2012;66: 493–520.

70. Burrows LL, Urbanic RV, Lam JS. Functional conservation of the polysaccharide biosynthetic protein WbpM and its homologues in Pseudomonas aeruginosa and other medically significant bacteria. Infect Immun. 2000;68: 931–936.

71. Veeranagouda Y, Lee K, Cho AR, Cho K, Anderson EM, Lam JS. Ssg, a putative glycosyltransferase, functions in lipo- and exopolysaccharide biosynthesis and cell surface-related properties in Pseudomonas alkylphenolia. FEMS Microbiol Lett. 2011;315: 38–45.

72. Kocíncová D, Ostler SL, Anderson EM, Lam JS. Rhamnosyltransferase genes migA and wapR are regulated in a differential manner to modulate the quantities of core oligosaccharide glycoforms produced by Pseudomonas aeruginosa. J Bacteriol. 2012;194: 4295–4300.

73. Melamed J, Kocev A, Torgov V, Veselovsky V, Brockhausen I. Biosynthesis of the Pseudomonas aeruginosa common polysaccharide antigen by D-Rhamnosyltransferases WbpX and WbpY. Glycoconj J. 2022;39: 393–411.

74. Whitchurch CB, Mattick JS. Characterization of a gene, pilU, required for twitching motility but not phage sensitivity in Pseudomonas aeruginosa. Mol Microbiol. 1994;13: 1079–1091.

75. Whitchurch CB, Hobbs M, Livingston SP, Krishnapillai V, Mattick JS. Characterisation of a Pseudomonas aeruginosa twitching motility gene and evidence for a specialised protein export system widespread in eubacteria. Gene. 1991;101: 33–44.

76. Ayers M, Sampaleanu LM, Tammam S, Koo J, Harvey H, Howell PL, et al. PilM/N/O/P proteins form an inner membrane complex that affects the stability of the Pseudomonas aeruginosa type IV pilus secretin. J Mol Biol. 2009;394: 128–142.

860 77. Webster SS, Wong GCL, O'Toole GA. The Power of Touch: Type 4 Pili, the von Willebrand A Domain, and Surface Sensing by Pseudomonas aeruginosa. J Bacteriol. 2022;204: e0008422.

78. Geiger CJ, O'Toole GA. Evidence for the Type IV Pili Retraction Motor PilT as a Component of the Surface Sensing System in Pseudomonas aeruginosa. bioRxiv. 2023.
865 doi:10.1101/2023.05.02.539127

79. Asikyan ML, Kus JV, Burrows LL. Novel proteins that modulate type IV pilus retraction dynamics in Pseudomonas aeruginosa. J Bacteriol. 2008;190: 7022–7034.

80. Azimi S, Thomas J, Cleland SE, Curtis JE, Goldberg JB, Diggle SP. O-Specific Antigen-Dependent Surface Hydrophobicity Mediates Aggregate Assembly Type in Pseudomonas
870 aeruginosa. MBio. 2021;12: e0086021.

81. Quan K, Hou J, Zhang Z, Ren Y, Peterson BW, Flemming H-C, et al. Water in bacterial biofilms: pores and channels, storage and transport functions. Crit Rev Microbiol. 2022;48: 283–302.

82. Meisner J, Goldberg JB. The Escherichia coli rhaSR-PrhaBAD Inducible Promoter System
875 Allows Tightly Controlled Gene Expression over a Wide Range in Pseudomonas aeruginosa. Appl Environ Microbiol. 2016;82: 6715.

83. McMackin EAW, Corley JM, Karash S, Marden J, Wolfgang MC, Yahr TL. Cautionary Notes on the Use of Arabinose- and Rhamnose-Inducible Expression Vectors in Pseudomonas aeruginosa. J Bacteriol. 2021;203: e0022421.

880 84. Webster CM, Shepherd M. A mini-review: environmental and metabolic factors affecting aminoglycoside efficacy. World J Microbiol Biotechnol. 2022;39: 7.

85. Hennes M, Bender N, Cronenberg T, Welker A, Maier B. Collective polarization dynamics in bacterial colonies signify the occurrence of distinct subpopulations. PLoS Biol. 2023;21: e3001960.

885 86. Walters MC 3rd, Roe F, Bugnicourt A, Franklin MJ, Stewart PS. Contributions of antibiotic penetration, oxygen limitation, and low metabolic activity to tolerance of Pseudomonas aeruginosa biofilms to ciprofloxacin and tobramycin. Antimicrob Agents Chemother. 2003;47: 317–323.

87. Ibberson CB, Barraza JP, Holmes AL, Cao P, Whiteley M. Precise spatial structure impacts
890 antimicrobial susceptibility of *S. aureus* in polymicrobial wound infections. Proc Natl Acad Sci U S A. 2022;119: e2212340119.

88. Radlinski LC, Rowe SE, Brzozowski R, Wilkinson AD, Huang R, Eswara P, et al. Chemical Induction of Aminoglycoside Uptake Overcomes Antibiotic Tolerance and Resistance in Staphylococcus aureus. Cell Chem Biol. 2019;26: 1355–1364.e4.

895 89. Pamp SJ, Gjermansen M, Johansen HK, Tolker-Nielsen T. Tolerance to the antimicrobial peptide colistin in Pseudomonas aeruginosa biofilms is linked to metabolically active cells, and depends on the pmr and mexAB-oprM genes. Mol Microbiol. 2008;68: 223–240.

90. Ciofu O, Tolker-Nielsen T. Tolerance and Resistance of Pseudomonas aeruginosa Biofilms to Antimicrobial Agents-How P. aeruginosa Can Escape Antibiotics. Front Microbiol.
900 2019;10: 913.

91. Bertani G. Lysogeny at mid-twentieth century: P1, P2, and other experimental systems. J Bacteriol. 2004;186: 595–600.

92. Shanks RMQ, Caiazza NC, Hinsa SM, Toutain CM, O'Toole GA. Saccharomyces cerevisiae-based molecular tool kit for manipulation of genes from gram-negative bacteria.
905 Appl Environ Microbiol. 2006;72: 5027–5036.

93. Schindelin J, Arganda-Carreras I, Frise E, Kaynig V, Longair M, Pietzsch T, et al. Fiji: an open-source platform for biological-image analysis. Nat Methods. 2012;9: 676–682.

94. Liao P-S, Chen T-S, Chung P-C, Others. A fast algorithm for multilevel thresholding. J Inf Sci Eng. 2001;17: 713–727.

910 95. Otsu N. A Threshold Selection Method from Gray-Level Histograms. IEEE Trans Syst Man Cybern. 1979;9: 62–66.

96. Virtanen P, Gommers R, Oliphant TE, Haberland M, Reddy T, Cournapeau D, et al. SciPy 1.0: fundamental algorithms for scientific computing in Python. Nat Methods. 2020;17: 261–272.

915 97. Migliori B, Datta MS, Dupre C, Apak MC, Asano S, Gao R, et al. Light sheet theta microscopy for rapid high-resolution imaging of large biological samples. BMC Biol. 2018;16: 57.

98. Tomer R, Ye L, Hsueh B, Deisseroth K. Advanced CLARITY for rapid and high-resolution imaging of intact tissues. Nat Protoc. 2014;9: 1682–1697.

920 99. Bria A, Iannello G. TeraStitcher - a tool for fast automatic 3D-stitching of teravoxel-sized microscopy images. BMC Bioinformatics. 2012;13: 316.

100. Takhar HK, Kemp K, Kim M, Howell PL, Burrows LL. The platform protein is essential for type IV pilus biogenesis. J Biol Chem. 2013;288: 9721–9728.

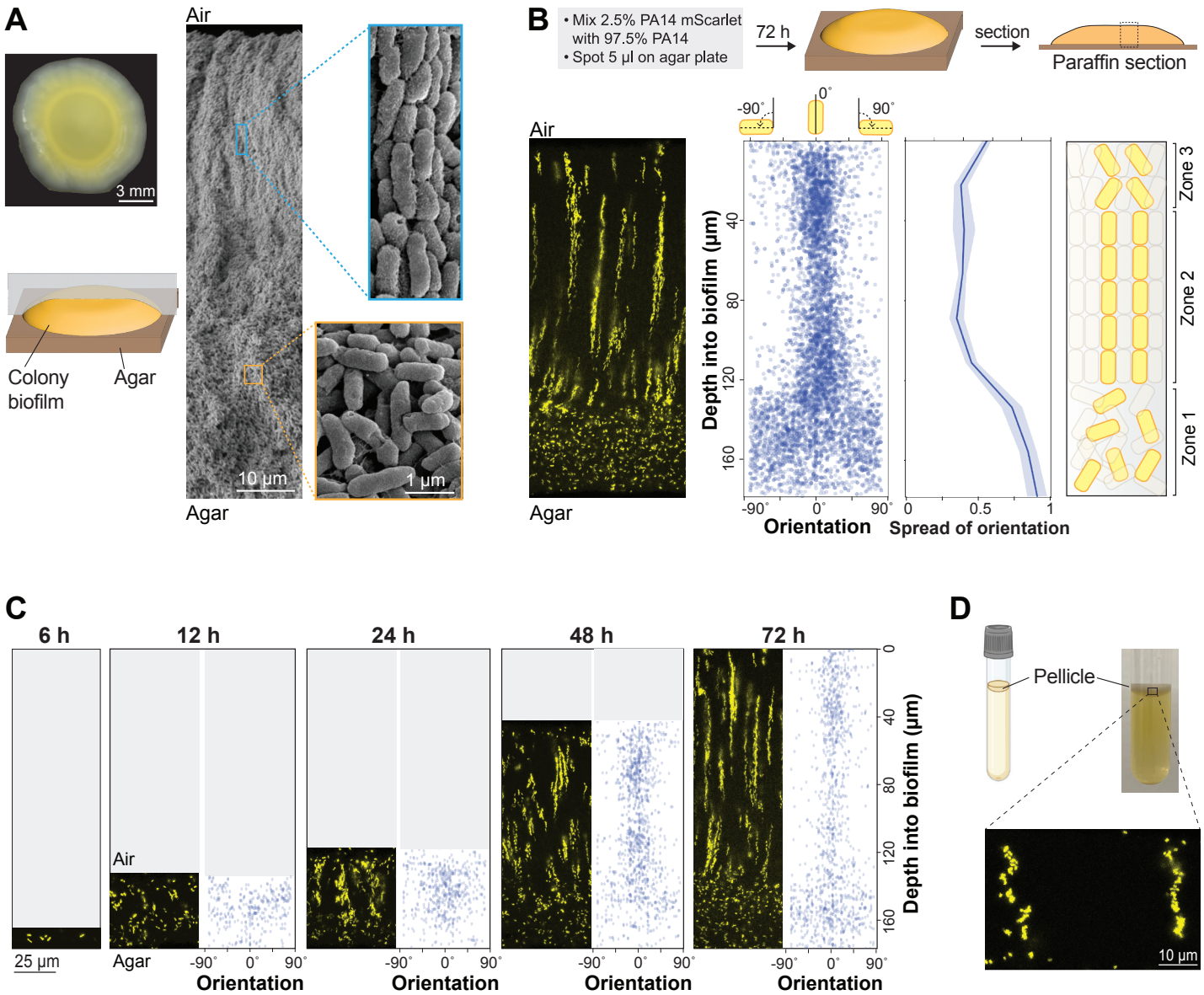

Figure 1. *P. aeruginosa* cells form vertical striations across depth in colony and pellicle biofilms. (**A**) **Left**: Top view of a *P. aeruginosa* colony biofilm grown for three days on 1% tryptone + 1% agar, and schematic showing orientation of the sample used for SEM imaging. **Right**: SEM images of a full colony biofilm cross-section. Insets of higher magnification show cellular arrangement and morphology for the indicated locations in the biofilm. (**B**) **Top**: Schematic of mixing assay method. **Left**: Fluorescence micrograph of a thin section prepared from a colony biofilm grown in the mixing assay. **Center**: Orientation across depth for fluorescent cells detected in biofilm thin section micrographs. The "spread of orientation" is the standard deviation of orientation values for each pixel across biofilm depth; the values shown in the plot are the average "spread of orientation" at each depth for thin section images taken from six biological-replicate biofilms. Shading represents the standard deviation for this average. **Right**: Schematic of cellular arrangement across depth in mature biofilms. (**C**) Micrographs of biofilms prepared as described in (B), but sacrificed at the indicated time points. (**D**) **Top**: Setup used to grow pellicle biofilms for microscopy. **Bottom**: Fluorescence micrograph of a thin section prepared from a pellicle biofilm. The inoculum contained 2.5% cells that constitutively express mScarlet. Images shown in this figure are representative of at least two independent experiments. mScarlet fluorescence is colored yellow.

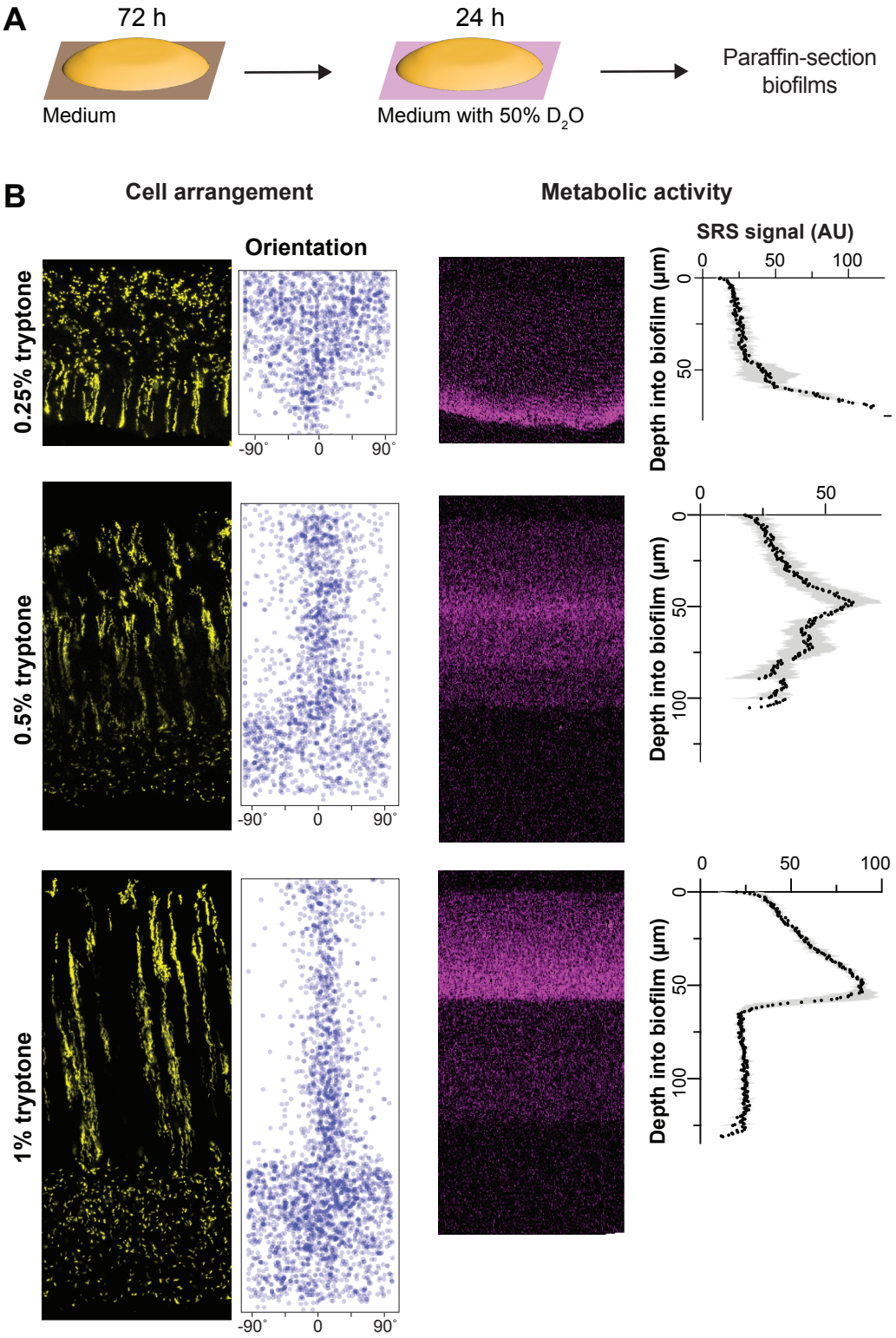

Figure 2. Resource availability affects the organization of cellular-arrangement zones and metabolic activity in biofilms. (**A**) Experimental setup for growing *P. aeruginosa* biofilms on agar plates and their subsequent transfer to medium containing D_2O for analysis of metabolic activity by stimulated Raman scattering (SRS) microscopy. (**B**) **Left**: Fluorescence micrographs and quantification of cellular orientation across depth for thin sections from mixing-assay biofilms grown on different concentrations of tryptone. **Right**: SRS microscopy images and SRS signal across depth for thin sections from mixing-assay biofilms grown on different concentrations of tryptone. SRS signal represents the average of three biological replicates with shading indicating the standard deviation.

A

Motility/cell surface associated	
Pilus	
pilB	*PA14_58750*
pilY1	*PA14_60310*
pilA	*PA14_58730*
pilT pilU	*PA14_05180, PA14_05190*
pilO	*PA14_66640*
Lipopolysaccharide/O-antigen	
ssg	*PA14_66120*
wapR	*PA14_66110*
wbpM	*PA14_23470*
Flagella	
cheY	*PA14_45620*
flgK	*PA14_50360*
motA motB	*PA14_65450, PA14_65430*
motC motD	*PA14_45560, PA14_45540*
Fimbrae	
cupA2	*PA14_37040*
cupD1	*PA14_59710*
ECM	
pelA-G	*PA14_24480 - PA14_24560*

Sigma factors	
rpoS	*PA14_17480*
rpoN	*PA14_57940*
fliA	*PA14_45630*

Second messengers	
c di-GMP	
dipA	*PA14_66320*
sadC	*PA14_56280*
bifA	*PA14_56790*
roeA	*PA14_50060*
rmcA	*PA14_07500*
wspR	*PA14_16500*
cAMP	
cyaA cyaB	*PA14_69610, PA14_22620*
cpdA	*PA14_65690*
(p)ppGpp	
relA	*PA14_52180*

Oxygen/NO-sensing	
aer1	*PA14_44300*
aer2	*PA14_02220*
aer1 aer2	*PA14_44300, PA14_02220*
nosP	*PA14_38990, PA14_38970*
anr	*PA14_44490*

Metabolism	
Phosphotransferase system	
ptsP	*PA14_04410*
ptsO	*PA14_57980*
Terminal oxidases	
ccoN1 ccoN2	*PA14_44370, PA14_44340*
ccoN1 ccoN2 ccoN4	*PA14_443470, PA14_44340, PA14_10500*
cco operons	*PA14_44340-PA14_44400*
Catabolite repression	
crc	*PA14_70390*
Pyruvate fermentation	
ackA	*PA14_53470*
ldhA	*PA14_52270*
ldhA ackA	*PA14_53470, PA14_52270*

Quorum sensing/virulence	
gacA	*PA14_30650*
lasR	*PA14_45960*
pqsA-C	*PA14_51430, PA14_51420, PA14_51410*
rhlR	*PA14_19120*
phz	*PA14_09480-PA14_09410, PA14_39970-PA14_39880*
antABC	*PA14_32160, PA14_32150, PA14_32140*
vfr	*PA14_08370*

B

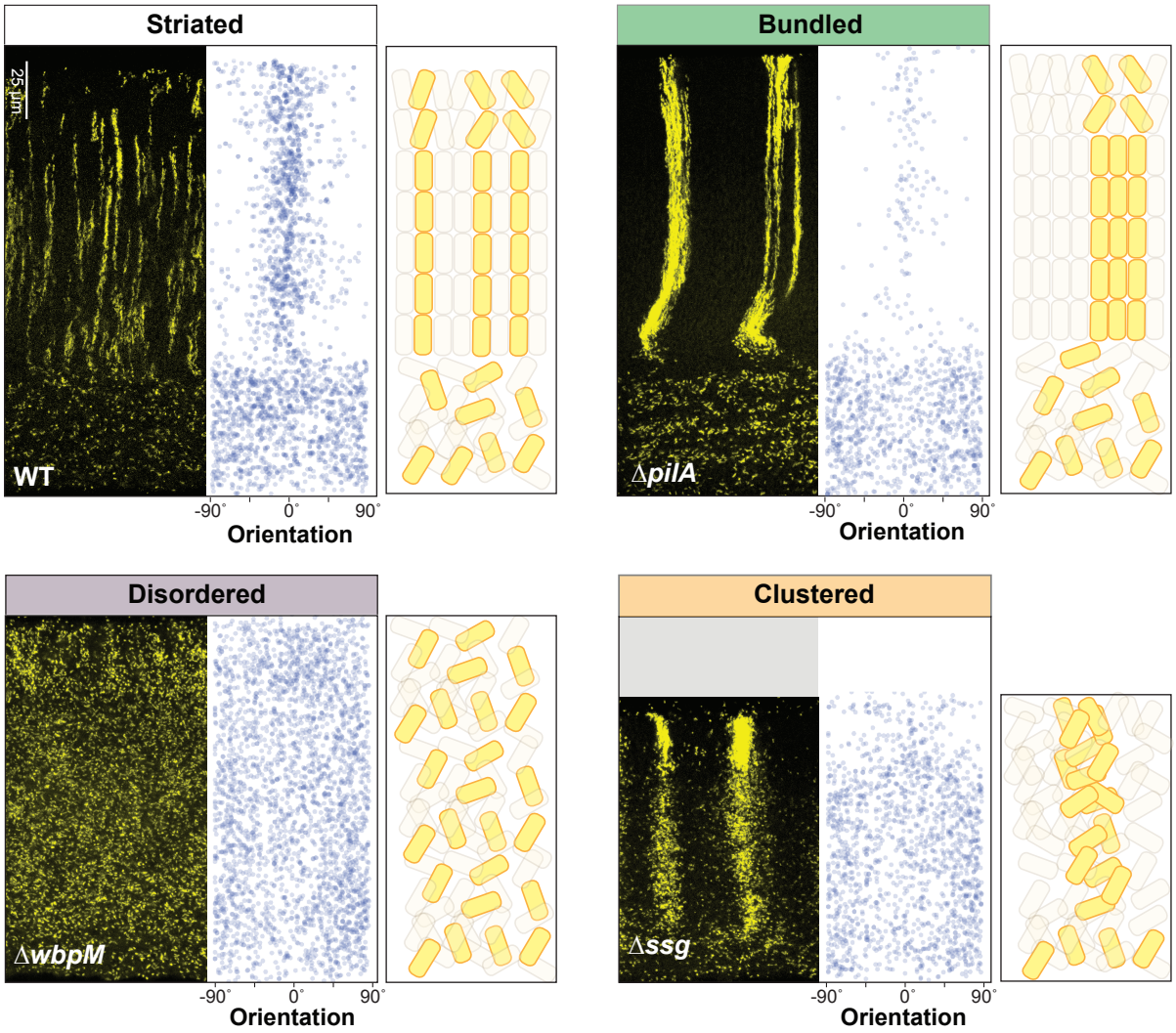

Figure 3. Specific global regulators and cell surface components are required for wild- type cell patterning in colony biofilms. (**A**) List of mutants screened for altered cellular arrangement across depth in biofilms. Those showing altered cellular arrangement are shaded and colors correspond to the phenotype categories shown in (B). (**B**) Fluorescence micrographs of thin sections from WT and indicated mutant biofilms grown on 1% tryptone + 1% agar for 3 days. Biofilm inocula contained 2.5% cells that constitutively express mScarlet. mScarlet fluorescence is colored yellow. Quantification of orientation across depth is shown for each image, and cartoons of cellular arrangement are shown for each phenotype category. Images shown are representative of at least two independent experiments.

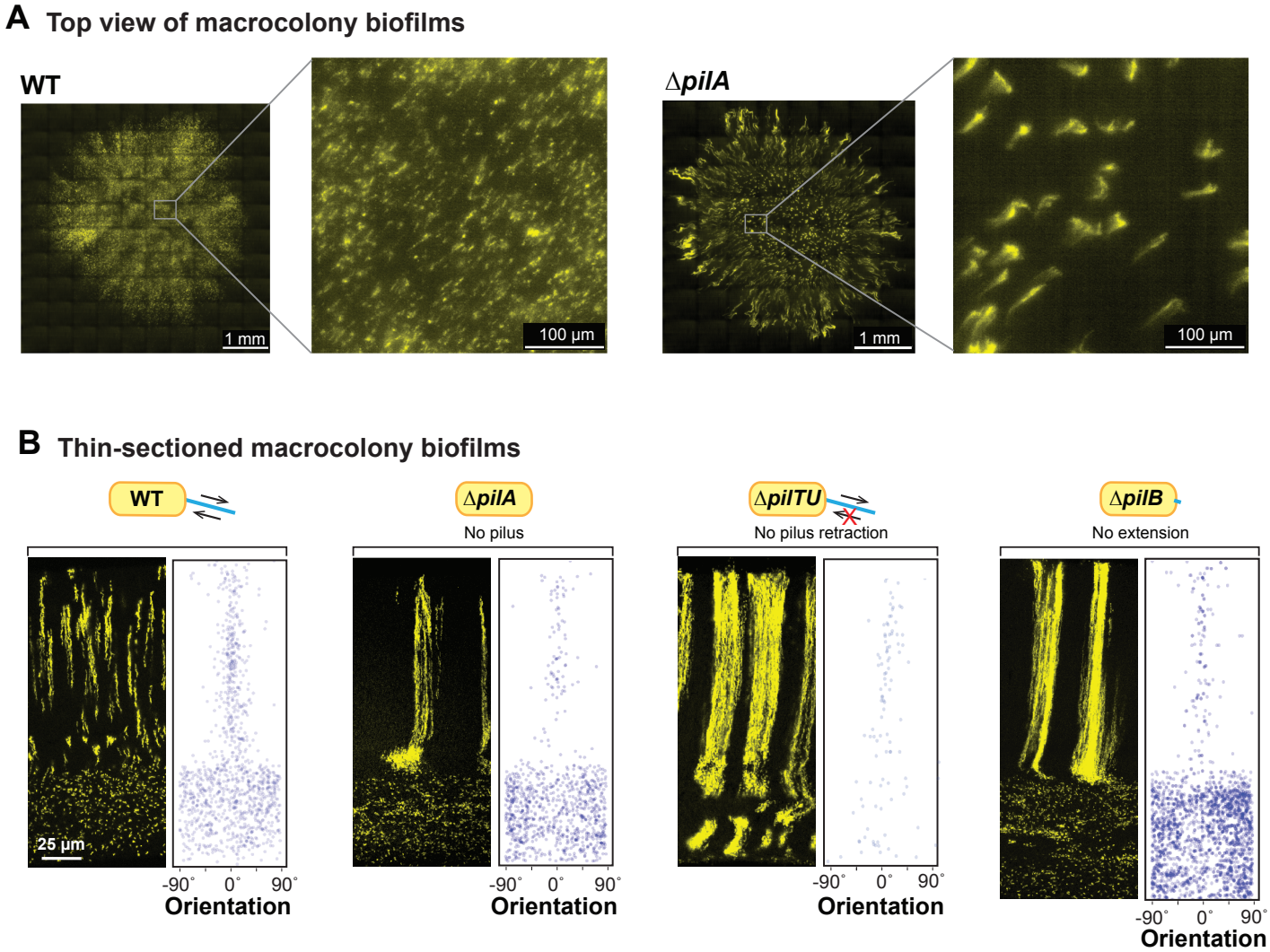

Figure 4. A retractable pilus is required for WT cellular arrangement. (**A**) High-resolution light sheet microscopy images of 19-hour old biofilms, with 1% of cells expressing fluorescent protein (colored yellow). (**B**) Fluorescence micrograph and quantification of orientation for WT and each of the indicated mutants grown in the mixing assay and thin-sectioned. The extent of pilus function present in each strain is indicated by a cartoon.

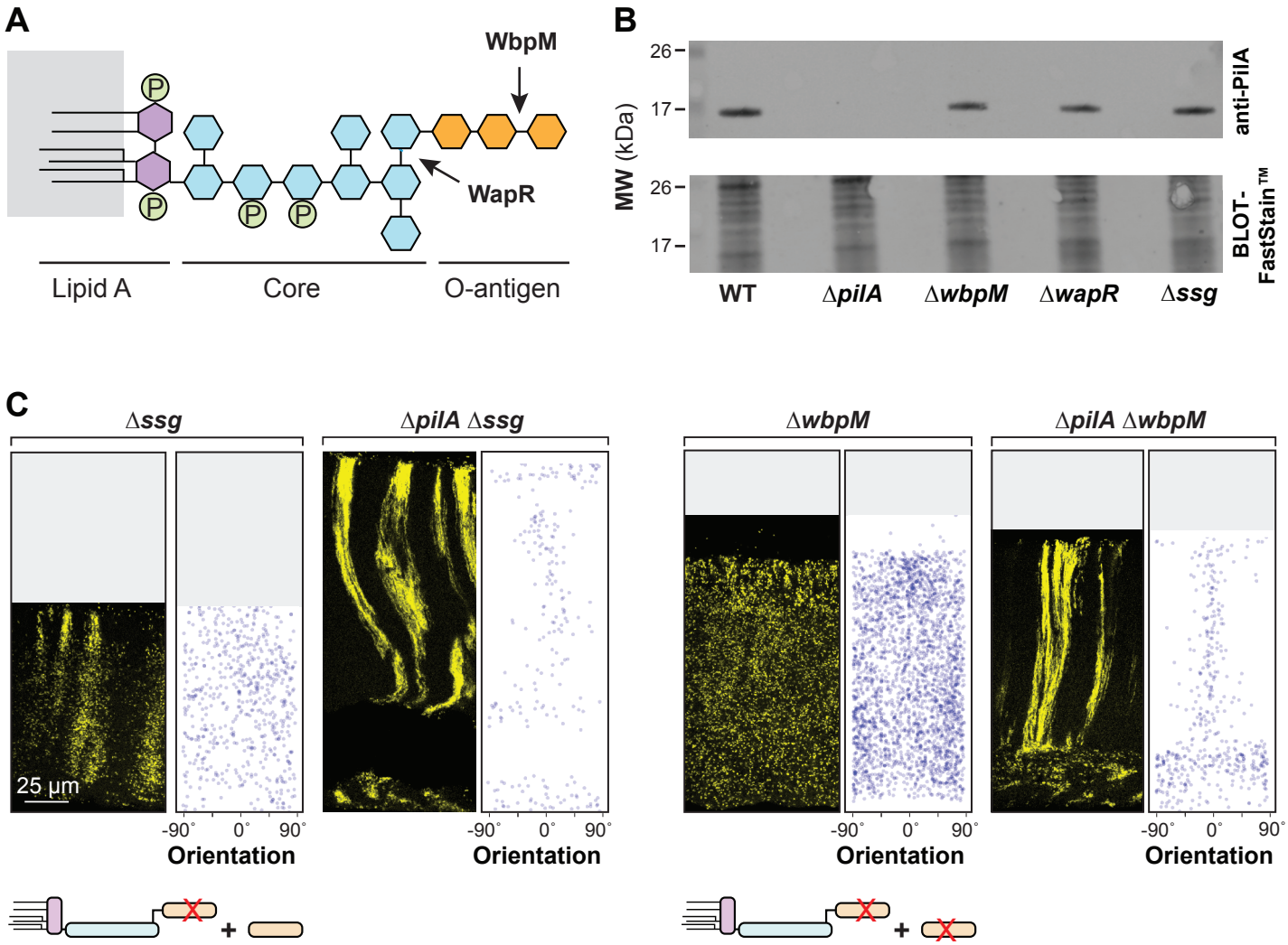

Figure 5. PilA is required for the disordered cellular arrangement phenotypes of O-antigen mutants. (**A**) Schematic of LPS and O-antigen indicating the bonds affected by WapR and WbpM activity. Hexagons represent monosaccharides and circles represent phosphate groups. The major components of LPS are color-coded. (**B**) Western blot showing PilA protein levels in macrocolony biofilms of WT and the indicated mutants. Equal amounts of total protein from sheared whole-cell lysates for each strain were resolved by SDS-PAGE using a 15% polyacrylamide gel. The PilA protein was detected using an anti-PilA antibody. (**C**) Fluorescence micrograph and quantification of orientation for each of the indicated mutants grown in the mixing assay and thin-sectioned. A cartoon representation of LPS and O-antigen (colors corresponding to panel (**A**)) indicates whether unattached and/or attached O-antigen are present in each strain. Images shown are representative of at least two independent experiments and mScarlet fluorescence is colored yellow.

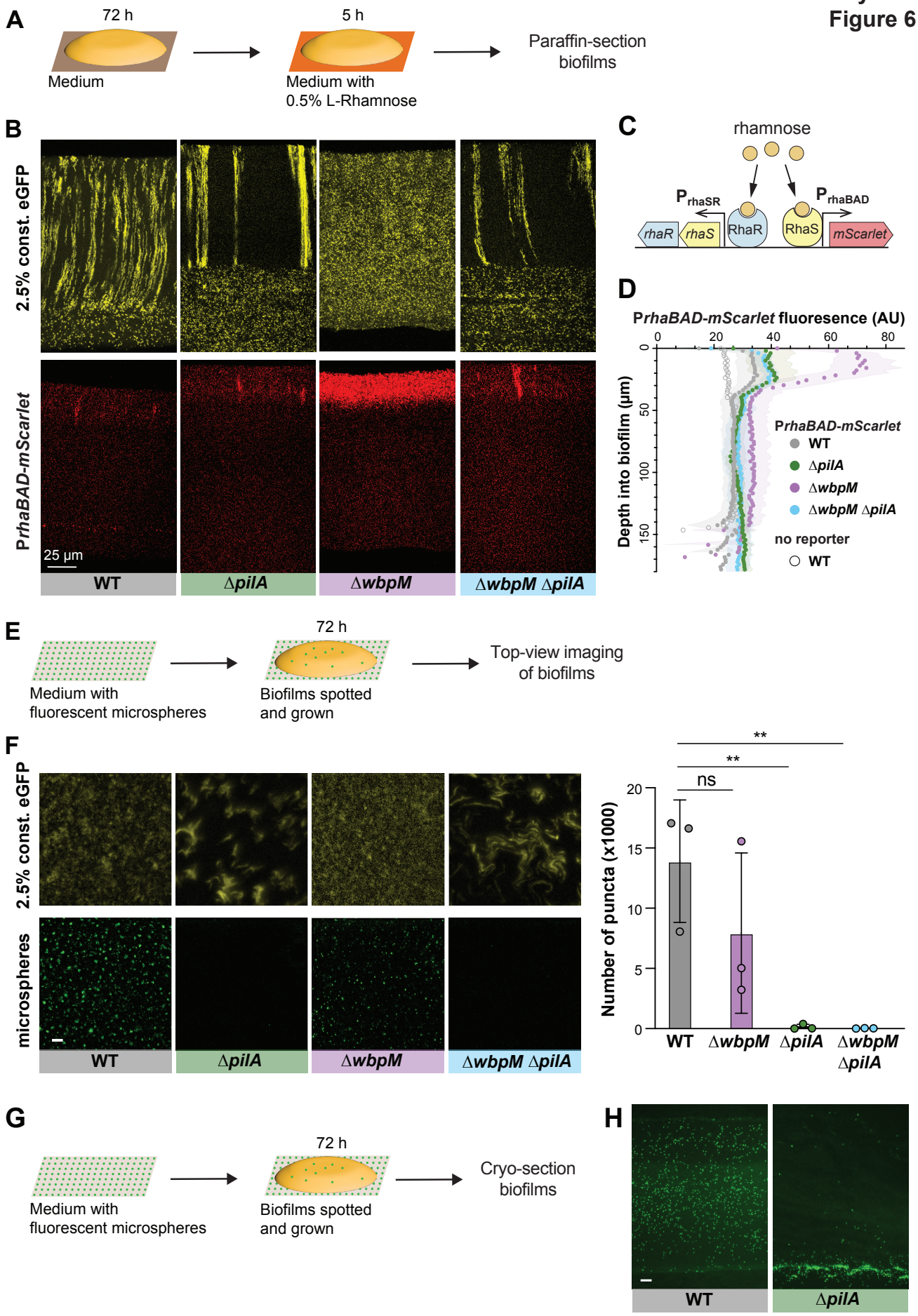
A
72 h
Medium
5 h
Medium with
0.5% L-Rhamnose
Paraffin-section
biofilms
B
2.5% const. eGFP
PrhaBAD-mScarlet
25 µm
WT
ΔpilA
ΔwbpM
ΔwbpM ΔpilA
C
rhamnose
PrhaSR
PrhaBAD
rhaR
rhaS
RhaR
RhaS
mScarlet
D
PrhaBAD-mScarlet fluoresence (AU)
0
20
40
60
80
Depth into biofilm (µm)
0
50
100
150
PrhaBAD-mScarlet
WT
ΔpilA
ΔwbpM
ΔwbpM ΔpilA
no reporter
WT
E
Medium with
fluorescent microspheres
72 h
Biofilms spotted
and grown
Top-view imaging
of biofilms
F
2.5% const. eGFP
microspheres
WT
ΔpilA
ΔwbpM
ΔwbpM ΔpilA
**
**
ns
Number of puncta (x1000)
20
15
10
5
0
WT
ΔwbpM
ΔpilA
ΔwbpM
ΔpilA
G
Medium with
fluorescent microspheres
72 h
Biofilms spotted
and grown
Cryo-section
biofilms
H
WT
ΔpilA

Figure 6. Cellular arrangement affects the uptake of substrates into colony biofilms. (**A**) Schematic illustration of the experimental setup for growing *P. aeruginosa* biofilms on agar plates and their subsequent transfer to medium containing L-Rhamnose. (**B**) Fluorescence micrographs of thin sections from WT and indicated mutant biofilms. Biofilm inocula contained 2.5% cells that constitutively express eGFP and 97.5% RhaSR-*PrhaBAD*-controlled mScarlet-producing strain. Top panels show eGFP fluorescence (colored yellow) and bottom panels show the mScarlet fluorescence for each thin section. (**C**) Schematic of RhaSR-P*rhaBAD* expression system driving mScarlet production. (**D**) Quantification of mScarlet fluorescence shown in (B). Shading represents standard deviation of biological triplicates. (**E**) Schematic of the experimental setup for growing *P. aeruginosa* macrocolony biofilms on agar plates with fluorescent microspheres (200 nm). (**F**) **Left**: Top-view images taken from center of macrocolony biofilms that were grown on medium with microspheres (colored green). Biofilms contained 2.5% cells constitutively expressing eGFP (colored yellow). **Right**: Quantification of microspheres visible in top-view images. Each data point is a biological replicate, bar height indicates the mean of these replicates. p values are based on two-sided unpaired t-tests (n.s., not significant; ** $p \leq 0.01$) Scale bar is 25 μm. (**G**) Schematic illustration of the experimental setup for growing biofilms on agar plates with fluorescent microspheres for cryosectioning. (**H**) Fluorescence micrographs of cryosections of biofilms grown on microspheres (colored green). Scale bar is 25 μm.

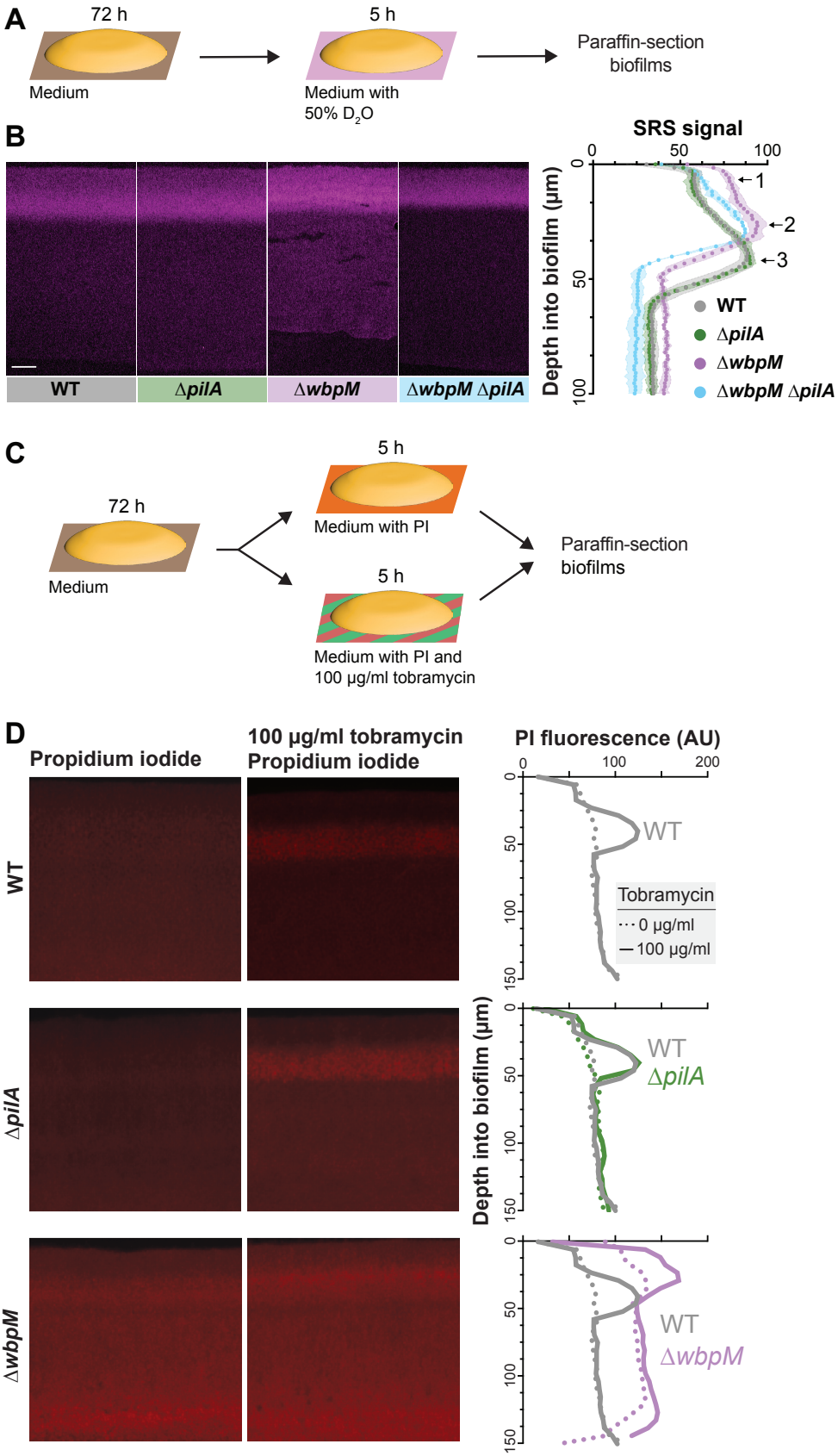
A
72 h
Medium
5 h
Medium with
50% D2O
Paraffin-section
biofilms
B
SRS signal
0
50
100
Depth into biofilm (µm)
0
50
100
1
2
3
WT
ΔpilA
ΔwbpM
ΔwbpM ΔpilA
WT
ΔpilA
ΔwbpM
ΔwbpM ΔpilA
C
72 h
Medium
5 h
Medium with PI
5 h
Medium with PI and
100 µg/ml tobramycin
Paraffin-section
biofilms
D
Propidium iodide
100 µg/ml tobramycin
Propidium iodide
PI fluorescence (AU)
0
100
200
WT
ΔpilA
ΔwbpM
Tobramycin
0 µg/ml
100 µg/ml
Depth into biofilm (µm)
0
50
100
150
WT
ΔpilA
WT
ΔwbpM

Figure 7. Mutations affecting cellular arrangement alter metabolic activity and antibiotic tolerance profiles within biofilms. (**A**) Schematic illustration of the experimental setup for growing biofilms on agar plates and their subsequent transfer to a medium containing D_2O for analysis of metabolic activity using SRS microscopy. (**B**) **Left**: SRS micrographs of WT and mutant biofilm thin-sections. Scale bar, 25 μm. **Right**: Graph showing the quantitative shift in metabolic activity distribution in different mutants. (**C**) Schematic illustration of the experimental setup for growing biofilms on agar plates and their subsequent transfer to a medium containing propidium iodide or propidium iodide + tobramycin (**D**) **Left**: Fluorescence micrographs of three-day-old biofilms exposed to propidium iodide (PI), a DNA stain. **Center**: Fluorescence micrographs of biofilms treated with tobramycin and PI. **Right**: Graphs showing quantification of PI staining. Images are representative of at least two independent experiments.